



# Compact and slender box concrete-filled stainless steel tubes under compression, bending, and combined loading

Sina Kazemzadeh Azad <sup>\*</sup>, Dongxu Li, Brian Uy

School of Civil Engineering, The University of Sydney, NSW 2006, Australia



## ARTICLE INFO

### Article history:

Received 18 January 2021

Received in revised form 8 June 2021

Accepted 14 June 2021

Available online 24 June 2021

### Keywords:

Stainless steel

Concrete-filled

CFSST

Design

Noncompact

Slender

## ABSTRACT

An extensive investigation on the behaviour of compact and slender box concrete-filled stainless steel tubular (CFSST) members is carried out studying their response under compression, bending, and combined compression and bending, with the main aim of developing comprehensive design procedures. Under this objective, an experimental programme is first conducted comprising compact and slender CFSSTs fabricated from austenitic and lean duplex stainless steel plates. Stub columns under axial compression as well as combined compression and bending, CFSST beams under pure bending, and long CFSST columns under axial force are all included in the experiments in order to investigate both the section and member responses. Specimens with high width-to-thickness ratios, high length-to-width ratios, and those under combined compression and bending are particularly considered in the experiments as test data is very scarce for such CFSSTs in the literature. A special technique is used to estimate the loads carried individually by the stainless steel section and the concrete infill to assist with the development of design recommendations. The experiments are followed by an extensive numerical study comprising over two hundred three-dimensional nonlinear finite element simulations. Outcomes of the experimental and numerical programmes are presented, analysed, and discussed thoroughly. Comprehensive procedures are then developed for the design of compact and slender CFSSTs under compression, bending, and combined loading which incorporate the effects of local and global buckling in strength predictions. Such procedures have not yet been established for CFSSTs in international design standards. The validity of the recommendations is demonstrated through comparison with the results of the present study as well as the test data available in the literature.

© 2021 Elsevier Ltd. All rights reserved.

## 1. Introduction

The ever-increasing importance of the life-cycle cost consideration for infrastructure and sustainable development has led to the increased use of stainless steel in structural applications. Compared to carbon steel, stainless steel possesses unique characteristics, such as high corrosion and fire resistance, that can be of great importance to engineers designing structures in corrosive environments [1,2]. The increasing use of stainless steel in practical applications has also significantly promoted the research on structural stainless steel in recent decades. This has in turn led to the development of design procedures which further facilitate the use of stainless steel members in buildings and bridges as main load-carrying elements [3–6]. The increased availability of a wide range of stainless steel grades in recent decades has also provided more opportunity for structural stainless steel applications [1]. Today, there are many structural applications of stainless steel in bridges

around the world [7] such as the Sölvaborg bridge in Sweden, the Helix bridge in Singapore, the Stonecutters cable-stayed bridge in Hong Kong, the Ruffolo bridge in Italy, the Cala Galdana bridge in Menorca, the Celtic Gateway bridge in Wales, and the recently-completed first stainless steel bridge of the United Kingdom over River Eamont in the village of Pooley Bridge.

Although the durability of stainless steel and its low maintenance cost have made it an attractive choice for engineers as well as decision-makers and owners, the main hurdle hampering its widespread structural use has always been its high initial cost [1,2,8]. Different approaches have been considered to lower the initial cost of stainless steel systems. The manufacturing process, for instance, is constantly evolving to lower the production cost and increase the price stability. Development of new grades, such as lean duplexes, with lower nickel content (to reduce nickel-related price fluctuations) is another step by the producers towards providing more economic stainless steel grades for structural applications [1,2]. Design methods have also been developed in recent years, for instance by Afshan and Gardner [9], to better exploit the significant strain hardening that stainless steel typically exhibits under plastic deformations.

\* Corresponding author.

E-mail address: [sina.kazemzadehazad@sydney.edu.au](mailto:sina.kazemzadehazad@sydney.edu.au) (S. Kazemzadeh Azad).

Another interesting approach that has been proposed to reduce the initial cost of stainless steel structures is the use of stainless steel in the composite form with concrete. Previous studies on concrete-filled (carbon) steel tubular (CFST) members have clearly demonstrated the advantages of composite columns in terms of enhanced strength, ductility, and constructability [10–14] compared to bare steel members. Consequently, in 2004, Roufegarinejad et al. [15] proposed the idea of concrete-filled stainless steel tubular (CFSST) columns. In concrete-filled tubes (CFTs) in general, the outer tube serves as permanent formwork for the concrete infill during construction as well as a confining mechanism during loading. On the other hand, the concrete infill increases the strength and stiffness of the column significantly and also enhances the local stability of the tube by preventing its inward buckling. In a CFSST, significant corrosion resistance is added to this efficient structural concept simply by utilising a stainless steel outer tube.

After the numerical study of Roufegarinejad et al. [15], the most comprehensive experimental studies on box CFSSTs were conducted by Young and Ellobody [16], Lam and Gardner [17], and Uy et al. [18] in the late 2000s. The experiments were chiefly conducted on austenitic stub columns under axial compression, with only a few tests on duplex specimens [16] or under combined loading [18]. It is worth noting that austenitic and duplex are the most commonly used stainless steel groups in structural applications [4]. In 2019, Lam et al. [19] reported the results of a series of axial compression tests conducted on lean duplex box CFSSTs. As noted earlier, lean duplex is a cost-effective member of the duplex group.

Yang and Ma [20] and Liao et al. [21] investigated the effects of using sea sand and recycled aggregate concrete infill on the axial behaviour of box CFSSTs. Yang and Ma [20] also extended their studies to box CFSST beams subjected to 4-point bending tests. Box CFSST beams with conventional concrete infill were also tested in 2017 by Chen et al. [22].

A few combined compression and uniaxial bending tests were conducted by Uy et al. [18]. They also conducted the first axial compression tests on long box CFSSTs [18]. In 2015, Tokgoz [23] tested long box CFSSTs with conventional and steel fibre concrete infill under compression and biaxial bending.

More recently, Kazemzadeh Azad et al. [24,25] investigated the local stability of concrete-filled and partially-encased stainless steel sections and proposed axial slenderness limits for austenitic, duplex, and lean duplex box CFSSTs based on a comprehensive experimental programme. The limits, which were found to be different than those developed for carbon steel CFSTs, could assist in categorising CFSSTs in terms of compactness and susceptibility to local buckling.

In addition to these experimental investigations, many numerical studies have also been conducted on the behaviour of box CFSSTs by researchers such as Ellobody and Young [26], Hassanein [27], Patel et al. [28], Tao et al. [29], and the authors [30]. Other aspects of CFSSTs, such as their fire performance, bond behaviour, and response under impact and cyclic loads, have also been investigated in the literature, a summary of which can be found in the recent comprehensive review study of Han et al. [31].

An outcome which is shared among the above-mentioned studies is that CFSSTs are viable alternatives to CFSTs, with significant advantages for structures located in corrosive regions. It is also frequently highlighted in these studies that the design rules developed mainly for carbon steel CFSTs are not directly applicable to CFSSTs and modifications are necessary in order to design safe and economic concrete-filled stainless steel members [24,31].

## 2. Motivation, objectives, and methodology

Although it has been acknowledged in many studies that modified design procedures are necessary to be developed for CFSSTs, there is still a significant lack of established methods in the literature for the design of these members. Two issues were identified as possible reasons for this. Firstly, in contrast to CFSTs [32,33], until recently, there was a

lack of research on the local buckling response of box CFSSTs. Understanding local buckling of elements is always essential for developing proper design guidelines for steel members. Secondly, although as outlined in Section 1 there has been some experimental studies on box CFSSTs, a review of the literature revealed that about 80% of the tests were conducted on stub columns under pure axial compression, chiefly considering small, compact sections. Consequently, the few design methods developed for box CFSSTs mainly focus on the pure compression case with limited applicability. Furthermore, some studies on other types of loadings (e.g. flexural bending), while providing valuable test data, have not provided any design recommendations. This is particularly the case for box CFSSTs with high width-to-thickness ratios which is important considering that CFSSTs are primarily intended for use in large infrastructure projects.

Consequently, a research programme was initiated at the University of Sydney to develop design guidelines for stainless steel-concrete composite members. In order to tackle the above-mentioned issues, the authors firstly investigated the local stability of CFSST members and recommended axial slenderness limits as well as effective width formulae [24,25]. In the second step, which is summarised in the present paper, a testing programme with compact and slender box CFSSTs under different loading conditions was considered. Details of the experimental study and the obtained results are presented in Sections 3 and 4, respectively. This is followed by a comprehensive numerical parametric study in Section 5. The experimental and numerical results are then combined with the test data available in the literature and synthesised in Section 6 to recommend design procedures for compact and slender box CFSSTs under compression, bending, and combined compression and bending. The conclusions of the study and a summary of the recommendations are presented in Section 7.

## 3. Experimental programme

### 3.1. Specimen selection and details

An important consideration in the test design process was to include not only the specimens which could provide comparability with previous test data available in the literature, but also specimens which were less-explored in previous studies. A careful examination of the literature revealed the scarcity (and in some cases lack) of available test data for box CFSSTs with high width-to-thickness ratios, high length-to-width ratios, and those under combined loading. This was particularly the case for duplex and lean duplex concrete-filled sections. This is illustrated in Fig. 1 where the specimens previously tested in the literature are summarised. All the experimental studies mentioned in Section 1 are also included in the dataset. The horizontal axis in the figure is the *relative slenderness* ( $\lambda = \sqrt{N_s/N_{cr}}$  where  $N_s$  is the section compressive strength and  $N_{cr}$  is the elastic buckling capacity of the member) which can be considered as a normalised measure of the length of the column, whereas the vertical axis is the *plate element slenderness* ( $\lambda_e = (b/t)\sqrt{f_y/250}$  where  $b$  is the internal width of the box section,  $t$  is the thickness, and  $f_y$  is the yield stress which is generally taken as the 0.2% proof stress ( $\sigma_{0.2}$ ) in materials without an apparent yield plateau such as stainless steel), as per AS/NZS 2327 [34], which is a normalised measure of the slenderness of the section. For bending-type tests, only the vertical axis is provided. It is worth noting that, following the Eurocode 3 [35] approach for stainless steel members, the plate element slenderness could also be defined as  $(b/t)\sqrt{f_y/250} \times \sqrt{E_s/210000}$ ; however, recent studies are recommending the use of a constant elastic modulus value ( $E_s$ ) for all stainless steel grades [4]. Considering this constant value in the above equations would lead to a minimal change in the plate element slenderness, and therefore, the original definition of  $\lambda_e$  was utilised in the present paper.

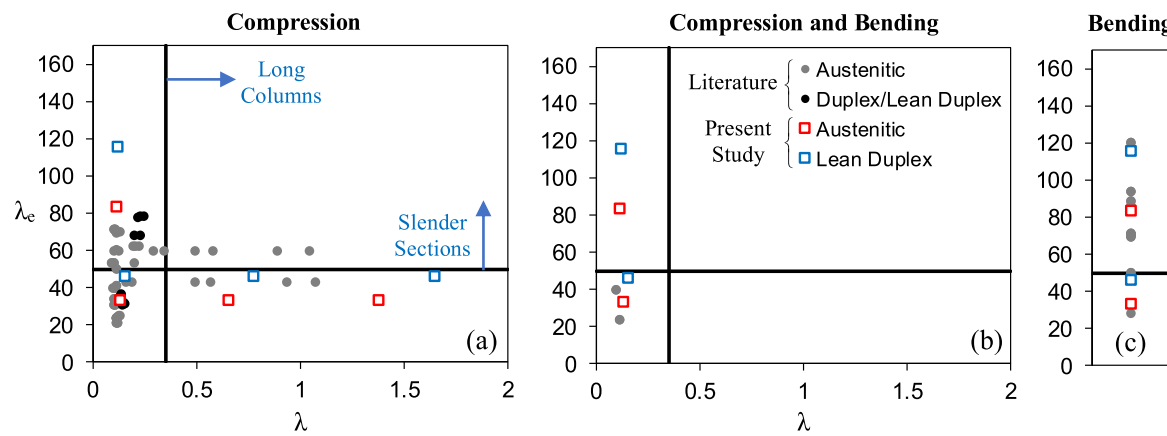


**Fig. 1.** Box CFSST specimens tested in previous studies and those in the present study.

Based on Kazemzadeh Azad et al. [24,25], a horizontal line at  $\lambda_e = 50$  is used in Fig. 1 to separate compact and slender sections, and a vertical line at  $\lambda = 0.35$  is used to tentatively separate stub and long column tests. Although there is no such a definitive threshold for long columns, this limit was selected as it approximately corresponds to about 10% loss of strength (compared to the section capacity) due to global buckling as per most international design standards [34,36,37].

According to Fig. 1a, most axial compression tests on box CFSSTs were conducted on compact sections or those with medium slenderness values. Tests on duplex/lean duplex CFSSTs are very limited, as well as those on long columns. Consequently, as shown in Fig. 1a, it was decided to test short box CFSSTs with a wide range of plate slenderness values ( $\lambda_e$ ), from compact to highly slender, to clarify the effect of local buckling on the section strength of these members. In addition, compact CFSSTs with different relative slenderness values ( $\lambda$ ) were included in the testing programme in order to investigate the global buckling behaviour. As shown in the figure, both austenitic and lean duplex sections were included in the tests. Compared to axial compression tests, the number of previous tests on box CFSSTs under combined compression and bending is extremely limited (Fig. 1b). Only two datapoints were found from the literature, which were both conducted on austenitic compact CFSSTs. Four new tests under combined compression and bending were therefore included in the present study considering austenitic and lean duplex, compact and highly slender sections. For the case of pure bending, as shown in Fig. 1c, there were some test data in

the literature for compact and slender austenitic box CFSSTs. However, there is a dearth of test data for duplex/lean duplex box CFSST beams. Consequently, both austenitic and lean duplex CFSST beams with compact and slender sections were included in the testing programme. It is worth mentioning that the limitations of the testing facility did not allow including some cases (e.g. long CFSSTs with slender sections) in the experimental programme. Their behaviour was however investigated via finite element (FE) analysis (Section 5).

Geometrical details of the selected specimens are summarised in Table 1. In line with the objectives of the study, four testing groups were considered: short columns under compression, beams under bending, short columns under combined compression and bending, and long columns under compression. The specimens are designated in the table with an **A** or a **D** based on their material (i.e. austenitic or duplex), followed by the nominal dimension of their internal width ( $b$ ), and a supplementary part based on their test type (**M**: bending test, **e**: eccentric test, and **L**: long column test). For instance, A100-e80 is an austenitic specimen, with a nominal internal width of 100 mm, tested under eccentric compression with an eccentricity ( $e$ ) of 80 mm (i.e. combined compression and bending). In addition to nominal dimensions, averaged measured dimensions of the specimens are also reported in Table 1. The thicknesses were measured from the coupons cut from the original plates (Section 3.2). Two lengths are presented in the table:  $\bar{L}$  which is the physical length of each specimen (Fig. 2), and  $L$  which is the length that should be used for design purposes. For

**Table 1**  
Details of the tested specimens.

Test Type	Specimen	Material	$b$ (mm)	$t$ (mm)	$\bar{L}$ (mm)	$L$ (mm)	$f_c$ (MPa)	$f_y$ (MPa)	$e$ (mm)
Compression (Short Columns)	A100	A304	100 [98.8]*	3 [3.07]	400 [399.0]	400 [399.0]	37	266	–
	A250	A304	250 [248.8]	3 [3.07]	850 [849.1]	850 [849.1]	37	266	–
	D100	LDX2101	100 [99.5]	3 [3.08]	400 [400.0]	400 [400.0]	37	511	–
Bending	D250	LDX2101	250 [249.5]	3 [3.08]	850 [850.2]	850 [850.2]	37	511	–
	A100-M	A304	100 [99.1]	3 [3.07]	1900 [1898.0]	1700 [1698.0]	37	266	–
	A250-M	A304	250 [249.6]	3 [3.07]	3950 [3944.8]	3750 [3744.8]	37	266	–
	D100-M	LDX2101	100 [99.5]	3 [3.08]	1900 [1899.0]	1700 [1799.0]	37	511	–
Compression and Bending	D250-M	LDX2101	250 [249.4]	3 [3.08]	3950 [3948.0]	3750 [3748.0]	37	511	–
	A100-e80	A304	100 [98.7]	3 [3.07]	400 [398.0]	524 [522.0]	37	266	80
	A250-e120	A304	250 [248.8]	3 [3.07]	850 [847.6]	1094 [1091.6]	37	266	120
Compression (Long Columns)	D100-e80	LDX2101	100 [99.3]	3 [3.08]	400 [398.2]	524 [522.2]	37	511	80
	D250-e120	LDX2101	250 [249.6]	3 [3.08]	850 [847.6]	1094 [1091.6]	37	511	120
	A100-L1.9	A304	100 [99.1]	3 [3.07]	1900 [1893.8]	2024 [2017.8]	37	266	–
	A100-L4.0	A304	100 [99.3]	3 [3.07]	4000 [3994.8]	4284 [4278.8]	37	266	–
	D100-L1.9	LDX2101	100 [99.5]	3 [3.08]	1900 [1893.6]	2024 [2017.8]	37	511	–
	D100-L4.0	LDX2101	100 [99.4]	3 [3.08]	4000 [3995.8]	4284 [4279.8]	37	511	–

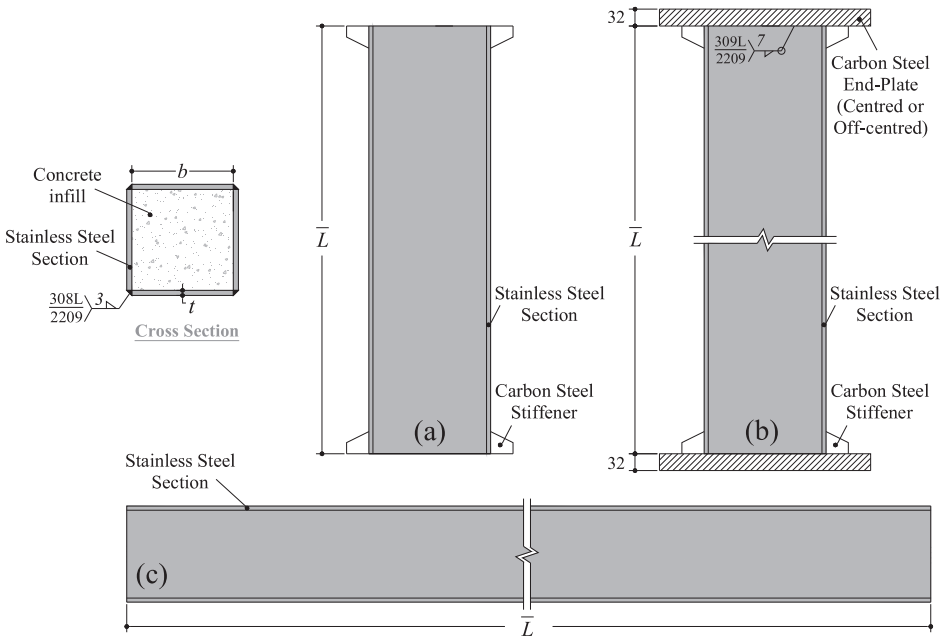


**Fig. 2.** Schematic view of the fabricated CFSST specimens: (a) short columns under compression; (b) long columns under compression, and short columns under combined compression and bending; and (c) beams under bending.

columns tested using knife-edges or pin connections,  $L$  is the length between the points of rotation, whereas for beams,  $L$  is the length between the supports. This is further elaborated in Section 3.4.

As schematically illustrated in Fig. 2, the specimens were fabricated in three types considering their test method. In all three types, the main stainless steel section was fabricated from four plates which were cut to size and fillet welded together using 308L or 2209 consumables (for austenitic and lean duplex specimens respectively). As shown in Fig. 2a, for short columns under axial force, only stiffeners were added and the specimen ends were ground flat after concrete casting. For long columns under compression, and short columns under compression and bending, in addition to stiffeners, 32 mm-thick carbon steel end plates were welded to the stainless steel section using 309L or 2209 consumables (Fig. 2b). This was necessary considering the utilised test setups (Section 3.4). For beams under bending, as shown in Fig. 2c, the fabricated stainless steel sections were directly used in the tests after concrete casting.

The 250 mm-wide columns and beams as well as the 4 m-long columns considered in the present study are some of the largest and most slender box CFSSTs tested to date. The specimens were also fabricated (or welded) sections which are less studied in the literature and could be the preferred choice (compared to cold-formed sections) in

large infrastructure projects where the use of stainless steel has significant advantages [7,38].

### 3.2. Material properties

As outlined in the previous section, it was essential to include both austenitic and duplex sections in the testing programme. Consequently, each specimen was fabricated from two stainless steel grades, namely, the austenitic grade 304/304L (EN 1.4301/1.4307) and the lean duplex grade LDX 2101 (EN 1.4162). These are respectively referred to as “A304” and “LDX2101” in Table 1. The 304 grade is the most commonly used austenitic grade. Lean duplexes, on the other hand, are cost-effective members of the duplex family with lower nickel content [4]. Their lower cost coupled with their high strength (similar to standard duplex grades) and reasonable corrosion resistance (similar to standard austenitic grades) have made them the preferred choice in many bridge applications [7,25].

The material properties of the utilised stainless steels were determined by tensile testing (as per AS 1391 [39]) of standard coupons cut in the longitudinal and transverse directions from the plates used in the fabrication of the specimens. The static material properties, summarised in Table 2, were determined following the procedure

**Table 2**  
Obtained material properties from stainless steel coupon tests.

Material	$t$ (mm)*	Coupon	Direction**	$E_s$ (GPa)	$f_y$ (MPa)	$f_u$ (MPa)	$\varepsilon_f$ (%)	$n$
Austenitic 304/304 L (EN 1.4301/1.4307)	3 [3.07]	A-L1	L	205.4	267	610	67	6.8
		A-L2	L	207.9	268	605	65	7.3
		A-T1	T	199.7	265	622	60	8.4
		A-T2	T	197.4	264	623	63	7.0
		Average		<b>202.6</b>	<b>266</b>	<b>615</b>	<b>64</b>	<b>7.4</b>
Lean Duplex 2101 (EN 1.4162)	3 [3.08]	LDX-L1	L	199.5	497	715	46	7.0
		LDX-L2	L	198.3	504	719	49	7.8
		LDX-T1	T	197.5	526	716	46	8.1
		LDX-T2	T	201.3	518	713	45	7.0
		Average		<b>199.2</b>	<b>511</b>	<b>716</b>	<b>46</b>	<b>7.5</b>

\* Both nominal and [measured] dimensions are reported.

\*\* L: Longitudinal (parallel to the plate rolling direction); T: Transverse (perpendicular to the plate rolling direction).

recommended by Huang and Young [40]. In the table, modulus of elasticity ( $E_s$ ), yield stress ( $f_y$ ) generally taken as the 0.2% proof stress ( $\sigma_{0.2}$ ) in materials without an apparent yield plateau, ultimate stress ( $f_u$ ), strain at fracture ( $\epsilon_f$ ), and Ramberg-Osgood parameter ( $n$ ) are reported for both grades. The obtained stress-strain ( $\sigma$ - $\epsilon$ ) curves as well as the averaged responses are presented in Fig. 3. As expected, round-type responses were observed for both grades. Very high levels of strain hardening and ductility ( $\epsilon_f > 60\%$ ) were recorded for the austenitic grade. The strain hardening of the lean duplex grade was lower while its ductility was still reasonably high ( $\epsilon_f > 40\%$ ). In both grades, relatively low levels of anisotropy were observed, particularly prior to necking. In general, the coupon test results were found to be very similar to those obtained previously by the authors from coupons of different thicknesses [24,25].

During concrete casting, a series of concrete cylinders of 150 mm diameter were also cast for material testing and cured as per AS 1012 [41]. Cylinders were tested every 7 days after the casting. Based on the average of the results obtained from testing five cylinders on the 28th day (which was also the start of the CFSST tests), the compressive strength of concrete ( $f_c$ ), elastic modulus of concrete ( $E_c$ ), and strain at maximum stress ( $\epsilon_{cu}$ ) were determined from standard compression tests on instrumented cylinders to be 37 MPa, 27.2 GPa, and 0.19%, respectively. The tensile strength of concrete ( $f_t$ ) was on the other hand obtained from splitting tests and found to be equal to 4.0 MPa. The results were reasonable considering the properties of the ordered concrete mix.

### 3.3. Geometrical imperfections

Local and global imperfections could have significant effects on the stability of CFSST members and their strength. Short specimens were used for measuring local imperfections while longer specimens were used for global imperfection measurements. It is worth mentioning that such measurements are rather limited in the literature for fabricated (or welded) stainless steel sections [24,25,38].

For local imperfection measurements, as shown in Fig. 4a, a laser-based measurement device was slowly moved across the width of the section with the help of a purpose-built rig and a stepper motor. On each side of the specimen, the measurement was repeated at five different sections along the length. Based on the classic definition of local imperfections for internal thin-walled elements [42], the magnitude of local imperfections at each side was then determined by comparing the measurement results with a reference line connecting the two corners of that side. The measured local imperfections for some of the specimens are depicted in Fig. 5a.

For global imperfections, on the other hand, the same measurement rig was used, however, two lasers were moved along the length of the specimen as shown in Fig. 4b. The lasers were mounted such that they would measure the imperfections along the corners of the section since, as suggested in the literature [43–45], corners of square sections

are, by definition, free from local imperfections, and therefore, best locations for measuring the global imperfections. The two measurements along the corners were first averaged and then corrected by removing the imperfections of the rig itself from the readings. As shown in Fig. 4c, this was done with the help of an automatic optical level with a parallel plate micrometre which measured the deviation of the line of movement of the lasers from a horizontal reference plane. This was deemed necessary to ensure that the measurements were not influenced by the imperfection of the rig itself. The results from the optical level showed a maximum deviation of 0.43 mm for the rig. This value is comparable to the global imperfections of the specimens. As recommended by Rasmussen and Hancock [46], the outlined procedure was then repeated for the other side of the specimen (by rotating it 180° about its longitudinal axis) and the obtained results from the two sides were averaged to eliminate the effects of gravity on the global imperfection measurements. Results for a representative case are shown in Fig. 5b.

The maximum absolute values of the measured local ( $\omega_l$ ) and global ( $\omega_g$ ) imperfections are summarised in Table 3. For better comparison, the reported values for the local cases are normalised with respect to the section width ( $b$ ) and for the global cases with respect to the length ( $L$ ). On average, the local imperfections were about  $b/500$  which is very similar to those measured previously by the authors [24,25] for a series of austenitic, duplex, and lean duplex box sections fabricated by two other fabricators in Australia. The magnitude is also lower than the fabrication tolerances stipulated by codes of practice for steel construction ( $b/125$  to  $b/250$ ) [47,48]. The global imperfections, on the other hand, were on average about  $L/5000$ . This is well below the limits considered in most codes of practice for steel construction ( $L/750$ ) such as AS/NZS 5131 [47] and EN 1090-2 [48], as well as the  $L/1000$  limit recommended in the new American draft code of practice for structural stainless steel construction, AISC 313 [49]. The implications of these global imperfection levels, as well as the effects of unintentional loading eccentricities on the global buckling of CFSSTs are discussed later.

### 3.4. Test setups and instrumentation

Testing for all the specimens was carried out in the J. W. Roderick Laboratory for Materials and Structures at the University of Sydney. Considering four different loading schemes in the experimental programme and including both compact and slender sections (Table 1) required using different test setups which are schematically illustrated in Fig. 6. For short columns under compression (Fig. 6e) specimen ends were ground flat after concrete casting and the load was applied using the loading platens of the machine. For the case of short columns under compression and bending (i.e. eccentric loading), as shown in Fig. 6d, end plates, which were welded to the specimen, were bolted to special loading platens which had knife edges and allowed for rotation about one axis. A similar setup was used for long columns with

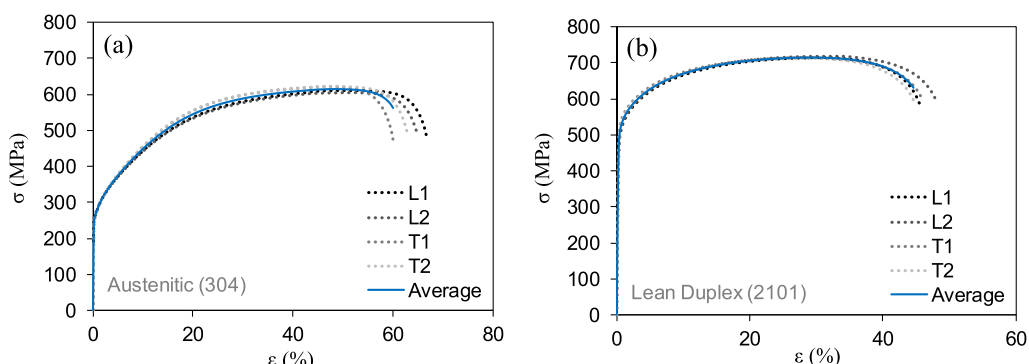
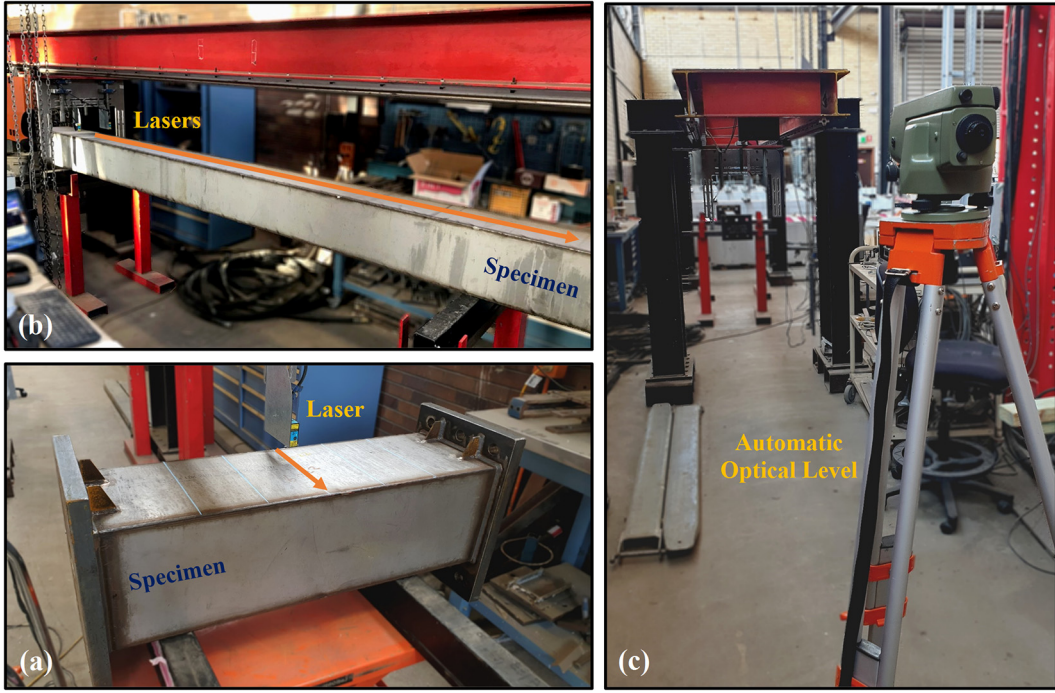


Fig. 3. Results of the coupon tests.



**Fig. 4.** Measurement of: (a) local imperfections; (b) global imperfections; and (c) imperfections of the rig itself.

$L = 2024$  mm, however, the load was applied concentrically (Fig. 6c). For the case of axially loaded very long columns with  $L = 4284$  mm, a tall frame was utilised. As shown in Fig. 6a, special pins were designed for the end connections to ensure the safety of the tests. In all of the column tests, loading was applied from one end while the other end of the specimen was fixed against longitudinal displacement. For the case of short column under compression (Fig. 6e), rotation of the loading

platens was also restrained. CFSST beams were tested in a four-point bending scheme as depicted in Fig. 6b. A loading beam was utilised to spread the point loads 500 mm apart from each other, causing the mid-region of the beam to be under pure bending.

The instrumentation used in each test setup is also summarised in Fig. 6. For all column tests (except very long columns, Fig. 6a) the net shortening of the column between the points of load application ( $\delta$ )

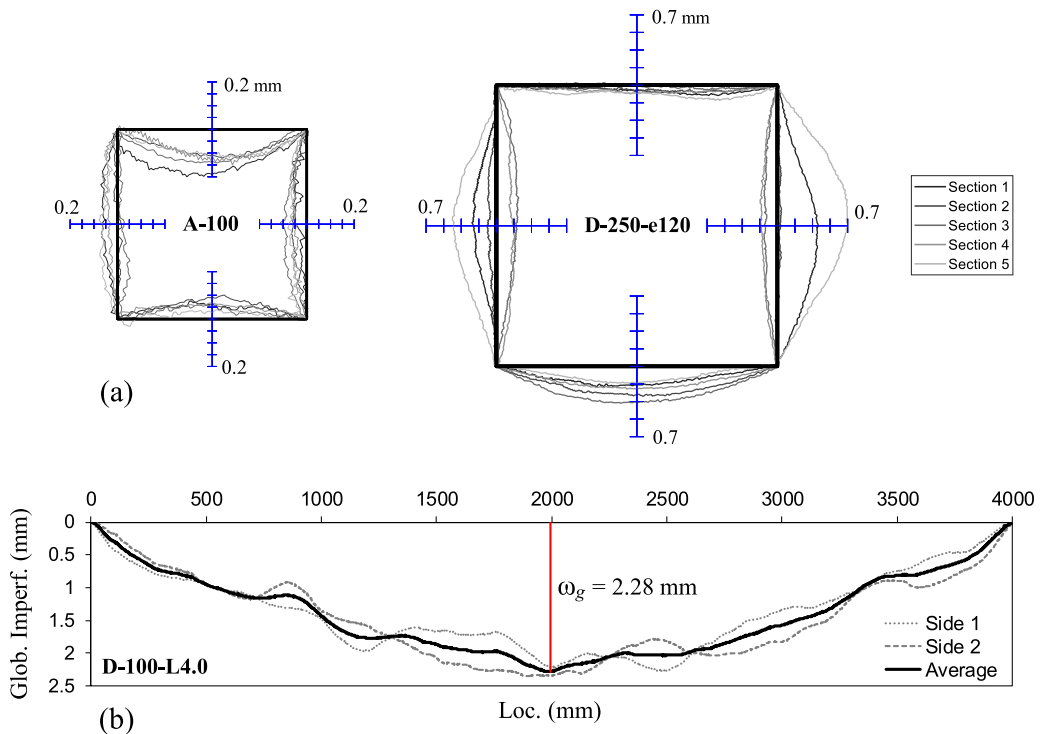


**Fig. 5.** Representative results for imperfection measurements: (a) local (magnified results); and (b) global.

**Table 3**

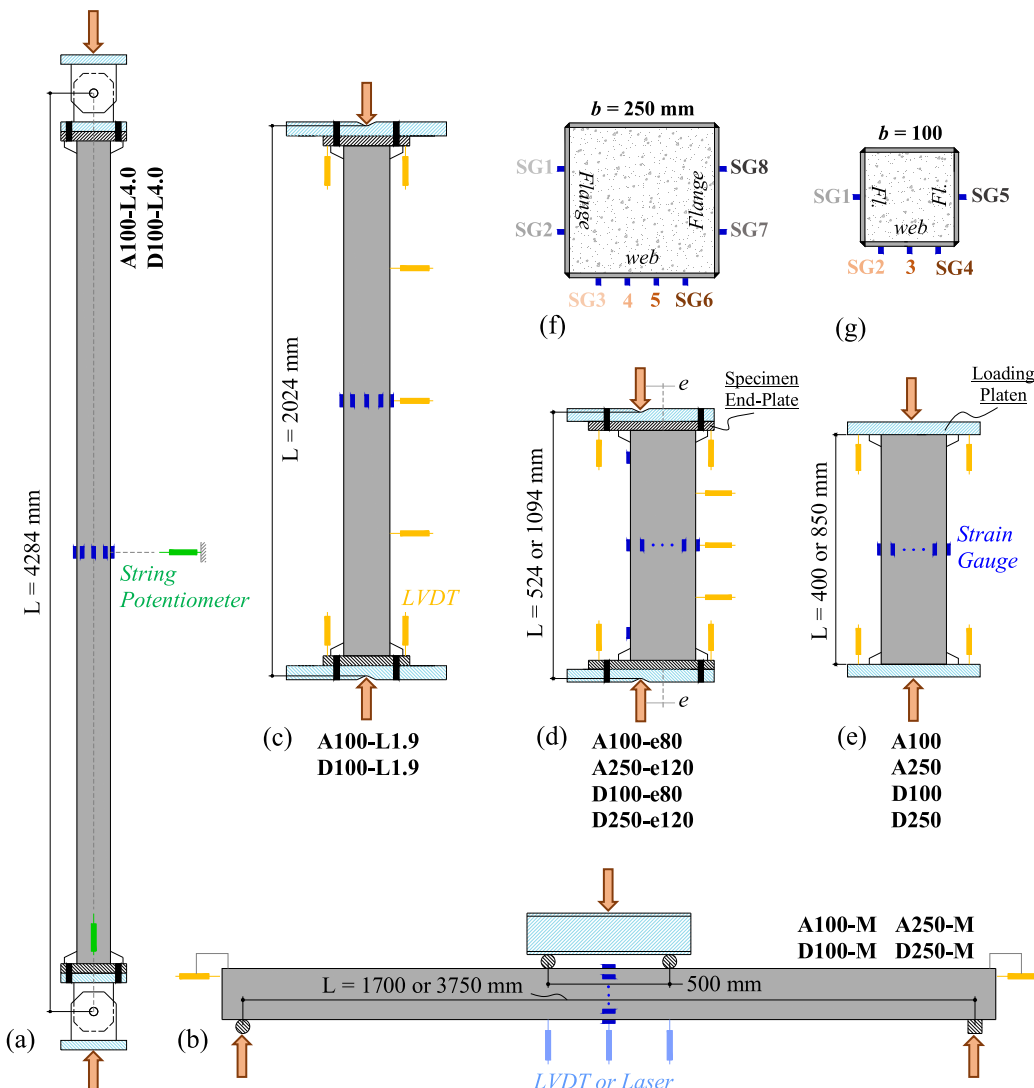
Imperfection measurement results.

Type	Specimen	$\omega_l$ (mm)	$\omega_l/b$	Type	Specimen	$\omega_g$ (mm)	$\omega_g/L$	$\omega_g + e_{load}$ (mm)
Local imperfection	A100	0.19	1/534	Global imperfection	A100-L1.9	0.56	1/3611	1.20
	A100-M	0.16	1/629		A100-L4.0	0.53	1/8139	0.45
	A250	0.54	1/462		A250-M	0.63	1/6371	–
	A250-e120	0.58	1/427		D100-L1.9	0.47	1/4339	1.50
	D100	0.18	1/553		D100-L4.0	2.28	1/1875	2.80
	D100-M	0.19	1/514		D250-M	0.70	1/5732	–
	D250	0.63	1/397					
	D250-e120	0.64	1/389					

was calculated based on the readings from four LVDTs located at specimen ends. For the case of long columns (Fig. 6c) and short columns under eccentric loading (Fig. 6d), the lateral displacements of the specimens were also measured with the help of three horizontal LVDTs. For the case of very long columns, on the other hand, as illustrated in Fig. 6a, string potentiometers were required to be used for determining the axial shortening between the pins and the lateral displacement at the mid-height. In the beam tests, three LVDTs (or laser-based measurement devices) were used in the mid-region to measure the deflection. An LVDT was also used at each beam end to measure the relative slip between the concrete infill and the stainless steel section (Fig. 6b).

Uniaxial strain gauges were also used in the experiments to capture the strain distribution at critical sections of the specimens. The typical arrangement used for the 250 mm- and 100 mm-wide sections is shown in Fig. 6f and Fig. 6g, respectively. Supplementary strain gauges, located close to the specimen ends on the compression side, were also used in eccentrically loaded tests, as shown in Fig. 6d.

During each test, the loading was continued until either a weld fracture was observed, or the resisted load reduced to 80% of the applied maximum load, whichever occurred earlier. The only exception was the beam specimens which showed a hardening-type response. In these specific specimens the test was continued until the strain at the

**Fig. 6.** Schematic view of the test setups and instrumentation used in the experiments.

extreme fibre reached a threshold value. This is discussed thoroughly in Section 4.3. All the specimens were tested quasi-statically and a data acquisition system was utilised to record the readings of the instrumentation.

#### 4. Experimental results

##### 4.1. Estimation of loads carried by stainless steel section and concrete infill

A critical issue identified in the early stages of this research was the importance of the correct estimation of the loads carried by the outer stainless steel section and the concrete infill during the tests. This is crucial in developing reliable design procedures for concrete-filled members, since, an ultimate section resistance obtained from a test can be interpreted differently by two researchers if the contribution of the outer section and the concrete infill to the total resistance is not known. For instance, one researcher can attribute more share of the total resistance to the stainless steel section, whereas the other researcher can assume a higher share for the concrete infill, and the formulae developed by the two would lead to the same ultimate section resistance at the end for that particular test.

While separating the loads carried by the outer stainless steel section and the concrete infill is relatively simple in a FE analysis [50,51], it is not as straightforward in experiments. An approach, used for instance by Uy [32,52], is to compare the experimental results for nominally identical steel sections which are tested under compression in different scenarios (hollow, concrete-filled, concrete-filled with steel

only loaded, etc.). The approach however requires multiple repeated tests which was not possible for the present study. Furthermore, application of this method to other loading types considered in this paper is rather complicated. Another approach proposed recently by Hu et al. [53] is to use a special end connection which permits the direct measurement of the load components. While being an interesting method, it is very difficult to be applied to the specimens and loading types considered in the present study.

Therefore, an alternative approach for measuring the load components of the tested CFSSTs was considered in the present study which relied on post-processing of the strain readings. To this end, the strain histories at the measurement points were fed into a MATLAB code which was developed to convert the strain histories to stress histories. Based on the estimated stress distribution at each timestep, a section integration was then performed to determine the compression ( $N^{st}$ ) and bending ( $M^{st}$ ) carried by the outer stainless steel section during the tests. The procedure is illustrated in Fig. 7. It should be emphasised that, although the tests were all monotonic, local strain reductions and reversals occurred frequently during the experiments due to failures and instabilities, and therefore, strains could not be translated to stresses simply by reading the corresponding stress value from the coupon test results. Instead, an incremental plasticity model with an *Elastic predictor-plastic corrector* scheme was required. Consequently, the 1D plasticity algorithm summarised in Fig. 7 was incorporated in the MATLAB code (based on Simo and Hughes [54] and Yaw [55]) as the tool for translating strains to stresses. In this algorithm,  $\varepsilon$ ,  $\varepsilon^p$ , and  $\sigma$  are the strain, plastic strain, and stress of the stainless steel section at the

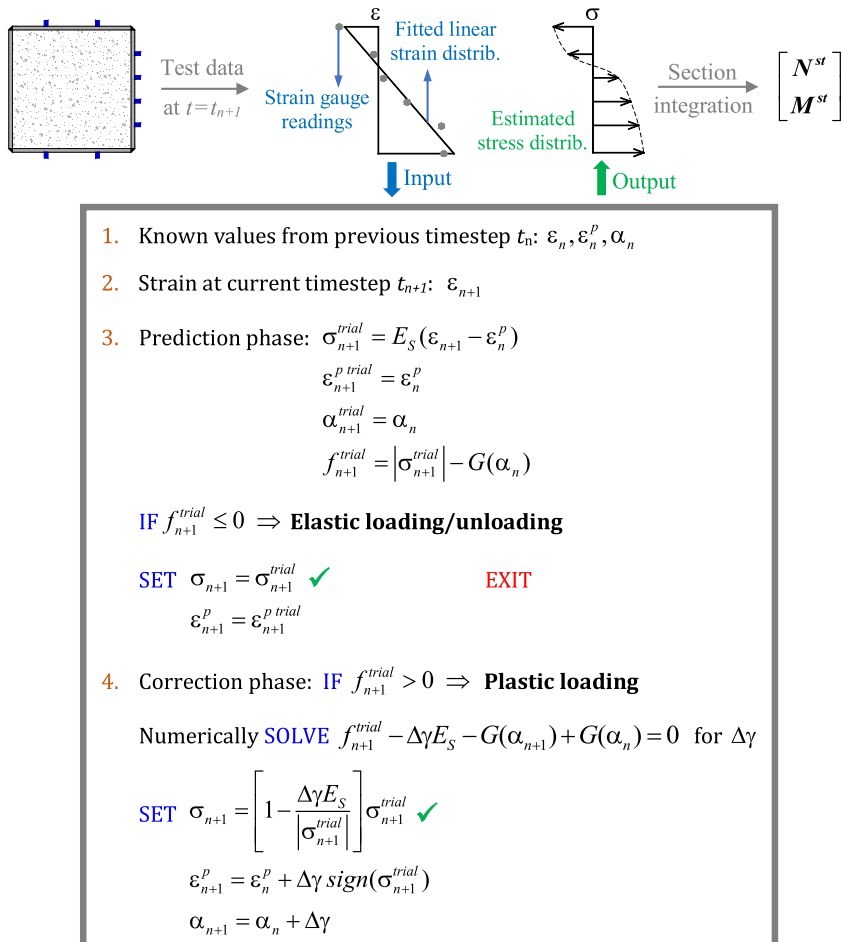


**Fig. 7.** The procedure for determining the compression ( $N^{st}$ ) and bending ( $M^{st}$ ) carried by the stainless steel section only.

measurement location;  $\alpha$  is the internal hardening variable; and  $G(\alpha)$  is the Ramberg-Osgood constitutive model which can be formulated as  $\sigma_o + C\alpha^m$  [56] where  $\sigma_o$  and  $m$  are material constants which are readily determined from the coupon test results (Section 3.2). In cases where the strain readings did not follow a strictly linear pattern, a line was fitted to the test data as illustrated in Fig. 7.

Once  $N^{st}$  and  $M^{st}$  were determined, the loads carried by the concrete infill could then be determined simply by subtracting the stainless steel share from the total compression and bending which were known from the load cell readings and statics (i.e. at each timestep  $N^{conc} = N - N^{st}$  and  $M^{conc} = M - M^{st}$ ).

The outlined method for determining the load components is only applicable until the failure of one (or more) of the strain gauges. This limit was found to be around 15,000  $\mu\epsilon$  for the utilised gauges and, for most cases, was sufficient for the purposes of the investigation. The results obtained from the outlined method are compared with those found from detailed FE analysis in Section 5.

#### 4.2. Short CFSSTs under axial compression

The obtained load-deformation curves for the tested CFSST stub columns under axial compression are presented in Fig. 8. In each subfigure, the total resisted force ( $N$ ) as well as the force resisted by the stainless steel outer section ( $N^{st}$ ) and that resisted by the concrete infill ( $N^{conc}$ ) are plotted based on the method outlined in the previous section. As it is seen, the approach provides the opportunity to trace the behaviour of the stainless steel section and the concrete infill individually, providing valuable insight into the behaviour of the specimens. In Fig. 8, three horizontal lines corresponding to the plastic axial capacity of the stainless steel section ( $A_s f_y$ ), plastic axial capacity of the concrete infill ( $A_c f_c$ ), and sum of these two plastic capacities ( $A_s f_y + A_c f_c$ ) are also included, where  $A_s$  is the area of the stainless steel section and  $A_c$  is the area of the concrete infill.

As shown in Fig. 8a and c, the investigated compact CFSSTs (A100 and D100), were able to reach their full plastic axial capacities. In these specimens, the stainless steel section experienced yielding which was followed by inelastic local buckling in the outward direction as shown in Fig. 9a. However, start of load reduction for the column typically coincided with the crushing of the concrete infill. This can be clearly observed in Fig. 8, where the reduction of  $N$  and the reduction

of  $N^{conc}$ , due to concrete crushing, occur almost simultaneously. This is an important advantage of using the method outlined in Section 4.1 for estimating the loads carried by the stainless steel section and the concrete infill, which allows for better identification of the concrete crushing instant. Although the noises heard during testing can be indications of the crushing, the considered approach is believed to be more accurate. Based on Fig. 8a and c, the concrete infill was able to reach to (and slightly exceed) its compressive strength in the tested compact CFSSTs. For the lean duplex D100 specimen, weld fracture also occurred at later stages of loading (at about 1.6% normalised axial shortening, i.e.  $\delta/L$ ), which is depicted in Fig. 9b and can be observed in Fig. 8c as a sudden drop in the axial load at the end of the test.

For slender CFSSTs (A250 and D250), on the other hand, the compressive resistance of the columns was observed to be notably lower than the corresponding plastic capacities. As it is seen in Fig. 8b and d, in these specimens, the slender stainless steel section could not achieve its yield strength due to premature local buckling. Compared to compact sections, this type of local instability (which is shown in Fig. 9d for a representative case) occurred at earlier stages of loading. In addition to this, as shown in Fig. 8b and d, the axial resistance of the concrete infill was found to be lower than  $A_c f_c$  in these CFSSTs. The size effect is considered to have played a role in this reduction in the concrete resistance. This is discussed in more detail in Section 6.1. The failure of the column and the initiation of load reduction were again marked by the crushing of concrete which can be identified from the  $N^{conc}$  curves in the figures. The results summarised in Fig. 8 also demonstrated that, after failure, the concrete infill rapidly lost its resistance while the stainless steel section exhibited a more stable response which contributed to the reserve strength of the column.

The total load vs stainless steel strain ( $N-\epsilon$ ) data for representative cases are plotted in Fig. 10a-b. As expected, all strain gauges followed a similar trend in the initial stages of loading as the column was under pure compression. For compact sections, such as D100 (Fig. 10a), the strain in the stainless steel section well exceeded the yield strain ( $\epsilon_y$ ) during the loading phase. It should be noted that  $\epsilon_y$  was calculated as  $0.002 + (f_y/E_s)$  considering the round-type material response of stainless steel and the use of  $\sigma_{0.2}$  as  $f_y$ . After the ultimate load, the redistribution of stresses due to concrete crushing and the occurrence of inelastic local buckling led to abrupt changes in the strain readings of some of the gauges and strain reversals in others. For the case of slender sections, as

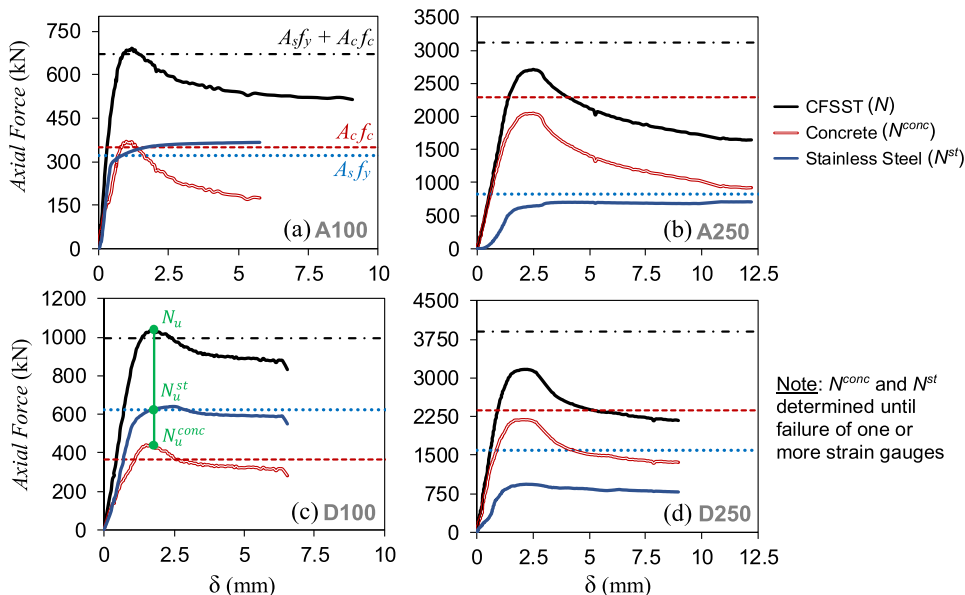
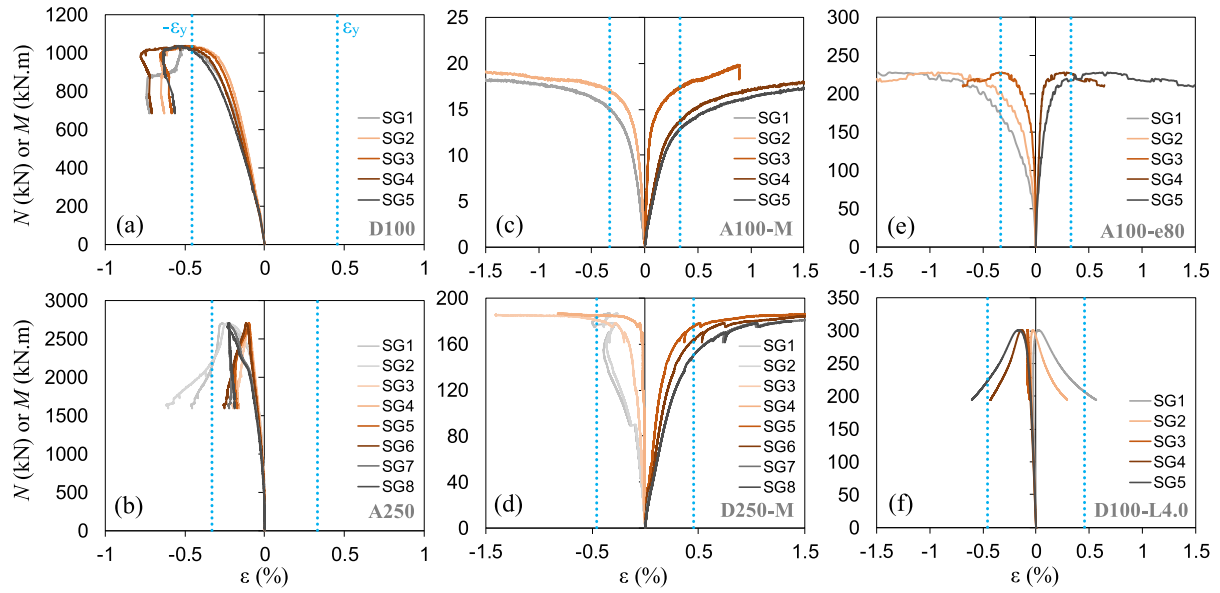


Fig. 8. Test results for short CFSST columns under compression.

**Fig. 9.** Specimens at the end of testing.

shown for instance in Fig. 10b for specimen A250, the strains during the loading phase remained below the yield strain, with some inconsistencies between the readings of the gauges which was due to the occurrence of premature local buckling. Abrupt changes were again recorded after concrete crushing which redistributed the stresses and exacerbated the local buckling-induced deformations.

Results for the short CFSST tests under axial compression are summarised in Table 4. In addition to the resisted ultimate load of each specimen ( $N_u$ ), the corresponding contribution of the stainless steel section ( $N_u^{st}$ ) and concrete infill ( $N_u^{conc}$ ) to this ultimate load are also reported. It should be emphasised that  $N_u^{st}$  and  $N_u^{conc}$  were not necessarily the maximum loads resisted by the stainless steel and concrete



**Fig. 10.** Axial load (or moment) versus strain curves (compressive strains: negative; tensile strains: positive). Refer to Fig. 6 for colour-coding of strain gauges and their location on the sections.

throughout the test, and instead, were the loads resisted by the stainless steel and concrete when the entire CFSST column was experiencing its ultimate load. This is illustrated in Fig. 8c for a sample case. This approach was necessary since the instant of ultimate load for a CFSST did not always coincide with that of its comprising parts.

#### 4.3. CFSST beams under flexural bending

Summary of the moment-deflection curves for the tested CFSST beams is presented in Fig. 11. The portion of the total moment ( $M$ ) carried by the stainless steel section ( $M^{st}$ ) and that carried by the concrete core ( $M^{conc}$ ) are separated in the figure based on Section 4.1. For comparison, a horizontal line corresponding to the plastic capacity of the CFSST beam ( $M_{pl}$ ) is also plotted. The additional horizontal lines  $M_{pl}^{st}$  and  $M_{pl}^{conc}$ , indicate the contribution of the stainless steel section and the concrete infill to  $M_{pl}$ . These limits are very useful in understanding the behaviour of the specimens; for instance, comparing  $M^{st}$  with  $M_{pl}^{st}$  can indicate whether the stainless steel section was able to attain its plastic capacity during the test or not. The limits were calculated based on a *plastic stress distribution method* (PSDM), which is illustrated

in Fig. 12a, considering a maximum concrete stress of  $f_{c,max} = f_c$ . According to the figure, for instance  $M_{pl}^{st}$  can be readily calculated as the moment of the stress distribution considered for the stainless steel section about the centroidal axis.

The studied compact CFSSTs were able to reach and significantly exceed their plastic moment capacities. As shown for instance in Fig. 11a for A100-M, the stainless steel section and the concrete core both attained their plastic capacities. For specimen D250-M with the highest section slenderness ( $\lambda_e = 116$ ), the full moment capacity of the beam was barely reached (Fig. 11d). This was mainly attributed to the premature local buckling of the top flange which prevented the development of  $M_{pl}^{st}$  in the stainless steel section as shown in Fig. 11d. Specimen A250-M performed better which could be attributed to its lower slenderness ( $\lambda_e = 84$ ) and higher degree of strain hardening of the austenitic grade. It should be noted that all the tested CFSST beams, the compact specimens in particular, exhibited a highly ductile flexural behaviour.

The typical failure mechanism observed for the studied compact CFSST beams included yielding of the bottom flange, yielding of the top flange coupled by inelastic local buckling (as shown in Fig. 9g), and finally crushing of the concrete in the compressive region. This

**Table 4**

Results of the experimental programme and FE verification (forces in kN and moments in kNm).

Test Type	Specimen	$\lambda_e$	$\xi$	$\lambda^*$	$N_u$	$M_u$	$N_u^{st}$	$N_u^{conc}$	$M_u^{st}$	$M_u^{conc}$	$N_u^{FE}$	$M_u^{FE}$	$N_u^{FE}/N_u$	$M_u^{FE}/M_u$
Compression (Short Columns)	A100	33	0.89	—	698.0	—	329.4	368.6	—	—	717.8	—	1.028	—
	A250	84	0.35	—	2709.0	—	655.2	2053.7	—	—	2850.2	—	1.052	—
	D100	46	1.71	—	1038.9	—	598.1	440.9	—	—	1040.3	—	1.001	—
	D250	116	0.68	—	3186.3	—	936.4	2249.9	—	—	3263.0	—	1.024	—
Bending	A100-M	33	0.89	—	—	17.4	—	—	12.7	4.6	—	16.9	—	0.971
	A250-M	84	0.35	—	—	107.7	—	—	74.5	33.2	—	103.4	—	0.960
	D100-M	46	1.71	—	—	30.3	—	—	23.8	6.4	—	30.5	—	1.007
	D250-M	116	0.68	—	—	187.3	—	—	128.3	58.9	—	181.3	—	0.968
Compression and Bending	A100-e80	33	0.89	—	228.0	18.2	—	—	—	—	217.0	18.2	0.952	1.000
	A250-e120	84	0.35	—	1065.3	130.6	—	—	—	—	1104.1	136.1	1.036	1.042
	D100-e80	46	1.71	—	358.9	29.2	—	—	—	—	345.2	29.3	0.962	1.003
	D250-e120	116	0.68	—	1207.2	154.0	—	—	—	—	1295.0	160.9	1.073	1.045
Compression (Long Columns)	A100-L1.9	33	0.89	0.7	595.3	—	254.9	340.4	—	—	575.1	—	0.966	—
	A100-L4.0	84	0.35	1.4	298.7	—	139.2	159.5	—	—	302.3	—	1.012	—
	D100-L1.9	46	1.71	0.8	801.6	—	418.0	383.6	—	—	753.2	—	0.940	—
	D100-L4.0	116	0.68	1.7	300.9	—	141.2	159.8	—	—	312.9	—	1.040	—

\* Reported only for long specimens.

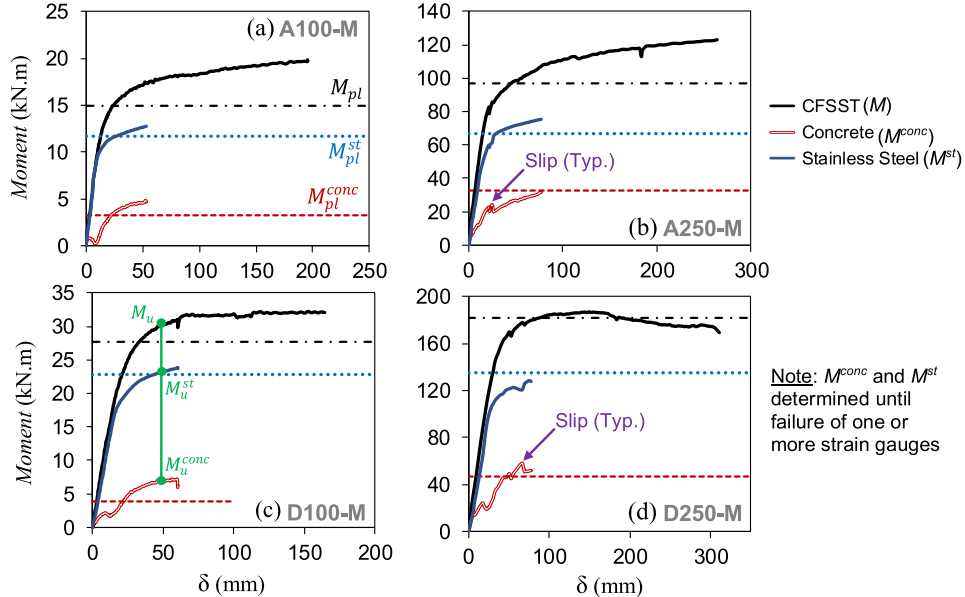


Fig. 11. Test results for CFSST beams under bending. Some typical instants of slip are indicated.

can be clearly observed from the strain data presented in Fig. 10c for A100-M. Strains in the top and bottom flanges rapidly passed the yield strain and the yielding gradually progressed through the web depth. On the contrary, as shown in Fig. 10d for D250-M with a slender section, while the bottom flange experienced yielding, the strains in the top flange could not reach  $\epsilon_y$  due to local buckling (Fig. 9j) which led to strain reversals in the corresponding gauges. Based on Fig. 10d, strain gauge #4 experienced minimal strains for a significant portion of the test since it was located close to the neutral axis. The gauge only activated after  $M \approx 180$  kN.m which marked the initiation of concrete crushing that shifted the neutral axis downwards resulting in a notable compression in strain gauge #4.

A small relative slip between the concrete and the stainless steel section was also observed in the CFSST beam tests, as shown in Fig. 9i. At the end of the testing, the slip was about 0.2–0.4 mm for the 100 mm-wide specimens, and about 2–3 mm for the 250 mm-wide beams. The occurrence of slip, which was generally accompanied by a distinctive noise during the tests, can also be observed as abrupt changes in the response of concrete (i.e. curve  $M_{concrete}$ ) in Fig. 11.

Tabulated results for the CFSST beam tests are presented in Table 4. Similar to the previous section, the ultimate moment resisted by the CFSST ( $M_u$ ), as well as the contributions of the stainless steel section ( $M_{st}^{st}$ ) and the concrete core ( $M_{u}^{conc}$ ) to this ultimate moment are reported. It should be noted that, in cases where the CFSST beam was found to have a hardening-type response (i.e. no apparent reduction

in the moment throughout the loading), a criterion was required for defining the ultimate point. Previous studies such as Han [57] and Yang and Ma [20] typically selected a threshold for the extreme fibre strain, mainly based on judgment, for defining such a criterion. In line with this, in the present paper, the ultimate state for CFSSTs with a hardening-type response was defined as the instant at which the extreme fibre strain reached to 1.5%. This was found to be a reasonable and conservative limit, considering the ductile response of CFSSTs and their strain hardening material characteristics. The same criterion was also used in the FE analyses of Section 5. The ultimate state and the corresponding moments are shown in Fig. 11c for a sample case.

It should be emphasised that there is currently a lack of a widely-accepted method for defining the ultimate moment for composite beams which exhibit a hardening-type response. While the above-discussed method of using a threshold for the extreme fibre strain has been used previously in the literature [20,57], it has a number of shortcomings. For instance, the length of the beam might influence the detection of the ultimate state as it could affect the rate of the strain development. Also, selection of the threshold value for the extreme fibre strain typically involves engineering judgment and can be somewhat arbitrary. As an example, a limit of 1% was used by Han [57] based on his tests on carbon steel CFST beams, noting that the moment appeared to stabilise after the extreme fibre strain reached this limit. The strain limit of 1.5%, which was used in the present study for CFSST beams, was also selected based on a similar approach. The limit

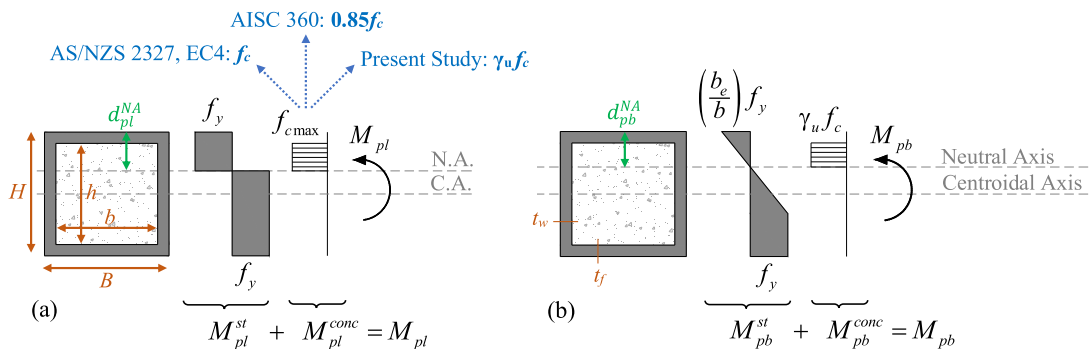


Fig. 12. (a) CFSST plastic moment capacity, and (b) proposed post-local buckling moment capacity for slender CFSSTs.

appeared more in line with the obtained test data and provided safe results with a reasonable level of conservatism. Interestingly, investigating the test data revealed that using the strain limit of 1% would have only led to a negligible change in the value of the ultimate moment for the tested specimens. In essence, while using a strain threshold for defining the ultimate moment has its drawbacks, until a better criterion is developed, this approach could be an option. Nevertheless, a study dedicated to developing a proper criterion appears to be necessary, at least for beams which exhibit a hardening-type response.

#### 4.4. Short CFSSTs under axial compression and flexural bending

Results for the short CFSSTs tested under combined compression and bending (i.e. eccentric loading) are summarised in Fig. 13. In each subfigure, the total axial force ( $N$ ) as well as the total moment ( $M$ ) resisted by the CFSST column are plotted. The left vertical axis in each subfigure corresponds to the axial force curve while the right vertical axis to the moment curve. The moment  $M$  was calculated as  $N \times (e + \delta_h)$  where  $e$  is the intentional load eccentricity and  $\delta_h$  is the horizontal displacement of the columns at its mid-height. In the combined loading tests, the loads carried by the stainless steel and the concrete infill cannot be directly compared with their plastic axial or bending capacities since each component of the CFSST can be under a combination of actions. Consequently, the  $N^{st}$  and  $N^{conc}$  curves are not included in Fig. 13.

The progress of failure observed for the eccentric loading tests was in fact a combination of those observed in the compression tests and bending tests. The specimens gradually bended with the application of the eccentric loading. Compared to the pure bending case, a larger portion of the section was under compression as the neutral axis was generally below the centroidal axis; which is evident from the strain gauge readings (Fig. 10e). This led to a quicker development of strains in the compressive flange compared to the tension flange. As a consequence, yielding and inelastic buckling of the compressive flange in the compact specimens (Fig. 9c), and premature local buckling of the compressive flange in the slender specimens (Fig. 9e) typically preceded yielding of the tension flange. Similar to the previous loading schemes, concrete crushing again marked the failure of the specimens, after which strength reduction started. The presence of larger strains in the compression flange (compared to the tension flange) resulted in weld fractures in all the specimens except A100-e80, due to severe local

buckling-induced deformations (e.g. Fig. 9c,e). The instant of weld fracture is evident in the plots of Fig. 13 as a sudden drop in the resistance of the specimen at the end of the experiments.

The ultimate axial force ( $N_u$ ) and bending moment ( $M_u$ ) resisted by the CFSST columns are summarised in Table 4. As shown in Fig. 13a, the ultimate point was defined based on the axial force (curve  $N$ ) and not the moment. The same approach was considered in the FE analyses of Section 5. It is worth noting that the results for the combined loading tests are also investigated in detail using  $N$ - $M$  interaction diagrams in Section 6.3.

#### 4.5. Long CFSSTs under axial compression

Strength of long columns is highly dependent on their initial imperfections. Consequently, an accurate estimation of the imperfections is crucial in correct interpretation of long column test results. Therefore, in addition to geometrical imperfections (Section 3.3), it was deemed necessary to also measure the unintentional loading eccentricity ( $e_{load}$ ) that the long CFSST columns were subjected to during the tests. A method used by Rasmussen and Hancock [46], He et al. [58], Buchanan et al. [59], and others for estimating  $e_{load}$  is to apply a relatively small elastic load (10–15% of the estimated failure load) to the column and use the strain readings to back-calculate the loading eccentricity. A similar approach was used herein where the total imperfection (i.e. global geometrical imperfection at mid-height plus the loading eccentricity) was estimated as follows based on statics and Euler–Bernoulli beam theory:

$$\omega_g + e_{load} = \frac{(EI)_{eff}(\varepsilon_{max} - \varepsilon_{min})}{N(b + 2t)} - \delta_h \quad (1)$$

where  $\varepsilon_{max}$  and  $\varepsilon_{min}$  are the strain gauge readings at extreme fibres and  $(EI)_{eff}$  is the effective flexural stiffness of the CFSST column. The general form of flexural stiffness for composite columns can be written as  $(EI)_{eff} = E_s I_s + \eta E_c I_c$  where  $I_s$  and  $I_c$  are the second moments of area of the stainless steel section and the concrete core, respectively, and  $\eta$  is a modification factor for the concrete contribution. International design standards recommend drastically different values for  $\eta$  [34,37,60]. In order to have an accurate estimate of the total imperfection, the factor  $\eta$  was determined using the following equation developed in the comprehensive study of Hu et al. [61]:

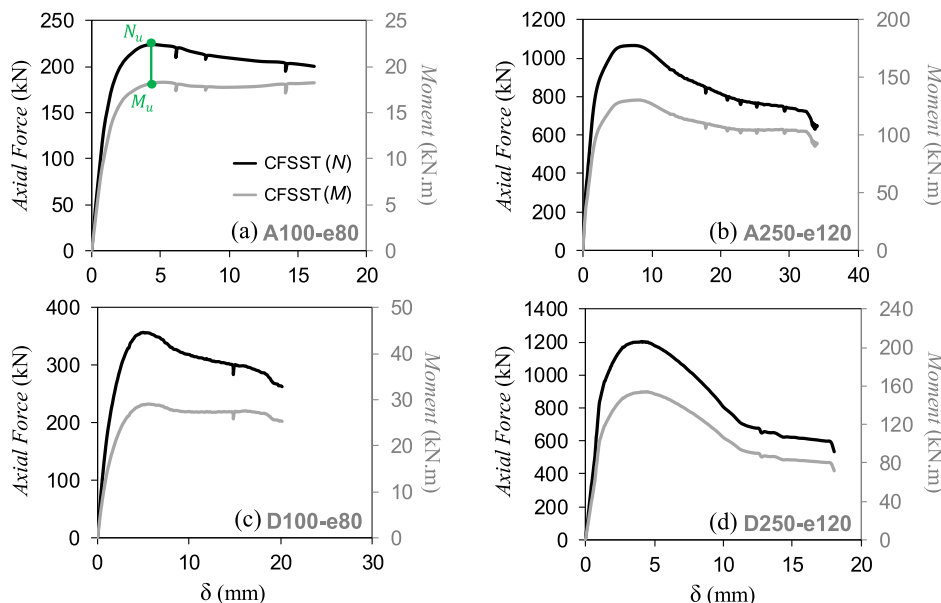


Fig. 13. Test results for short CFSST columns under compression and bending.

$$0 \leq \eta = \frac{E_s A_s - 2N E_s / f_y}{0.85 E_c A_c + 2E_s A_s} \leq 1.0 \quad (2)$$

It should be emphasised that this equation was only used for the purpose of estimating the total imperfection of the tested long columns, whereas in the design-related discussions of Section 6.4 the codified  $\eta$  values were used. If the axial force  $N$  is not known a priori, Eq. (2) requires an iterative analysis process, which is not straightforward for design purposes. Based on the outlined method, the total imperfection ( $\omega_g + e_{load}$ ) for the long CFSST specimens were calculated (Table 3). It was noted that in some cases  $e_{load}$  and  $\omega_g$  were in the same direction whereas in others they were in opposite directions.

Test results for the long CFSSTs are summarised in Fig. 14 and Table 4. As it is seen from the figure, due to global buckling, specimens failed at a lower load compared to their section squash load. While long specimens A100-L1.9 and D100-L1.9 experienced inelastic global buckling, the very long specimens A100-L4.0 and D100-L4.0 exhibited elastic global buckling. This is evident from the strain data of Fig. 10f where, prior to the ultimate load, none of the strain gauges reached to the yield limit. After global buckling, however, the gauges on the tension and compression sides experienced rapid straining going into the plastic region.

As shown in Fig. 9f, in long specimens A100-L1.9 and D100-L1.9, local buckling was also observed in addition to global buckling. On the other hand, as shown in Fig. 9h, the tested very long CFSSTs (A100-L4.0 and D100-L4.0) exhibited only global buckling which was accompanied by a significant lateral deformation. Most of the lateral deformation was however elastically recovered when the load was gradually removed.

## 5. Numerical programme

### 5.1. Modelling details

#### 5.1.1. Element types and meshing

All numerical simulations considered material and geometrical nonlinearities and were carried out using ABAQUS 6.14–1 [62]. Four-node

S4R shell elements with 9 through-thickness integration points were used for the modelling of the stainless steel section, and eight-node C3D8R brick elements for the concrete core. Based on the recommendations available in the literature [24,30,63], the mesh size was selected approximately as  $b/15$  across the section, and  $L/100$  along the length of the specimens. The mesh size was found to provide accurate results compared to the test results, with a reasonable computational cost, and further refinement of the mesh was found to be unnecessary.

#### 5.1.2. Material behaviour

The von Mises plasticity constitutive model of ABAQUS was used in all the analyses of the present study for simulating the material behaviour of the A304 and LDX2101 stainless steel grades. The elastic modulus ( $E_s$ ) was taken as 202.6 GPa and 199.2 GPa for the austenitic and lean duplex grades, respectively, based on the average of the coupon test results summarised in Table 2. The constitutive model also required the true stress versus true plastic strain ( $\sigma_{tr} - \varepsilon_{tr}^p$ ) response of the material to be defined. To this end, the average engineering stress-strain ( $\sigma - \varepsilon$ ) curves obtained from the coupon tests (Fig. 3) were first converted to ( $\sigma_{tr} - \varepsilon_{tr}^p$ ) data, using the following formulae, and then used as input for the von Mises plasticity constitutive model:

$$\sigma_{tr} = \sigma(1 + \varepsilon) \quad (3)$$

$$\varepsilon_{tr}^p = [\ln(1 + \varepsilon)] - \frac{\sigma_{tr}}{E_s} \quad (4)$$

For the concrete infill, the Concrete Damaged Plasticity (CDP) model of ABAQUS was used. Details of the compressive and tensile responses of concrete were required as input for this material model. In order for the CDP model to properly capture the confinement effects on the softening behaviour and lateral expansion of passively-confined concrete, special stress-strain responses (instead of that from an unconfined cylinder test) are typically required in CFT modelling [63–65]. To this end, the approach developed by Tao et al. [63] and widely used in the literature [51,66,67] was considered herein, with a minor modification. The main parameters of the concrete model are summarised in Fig. 15. In addition to these, the flow potential eccentricity ( $e_{pot}$ ), dilation angle ( $\psi$ ), ratio of

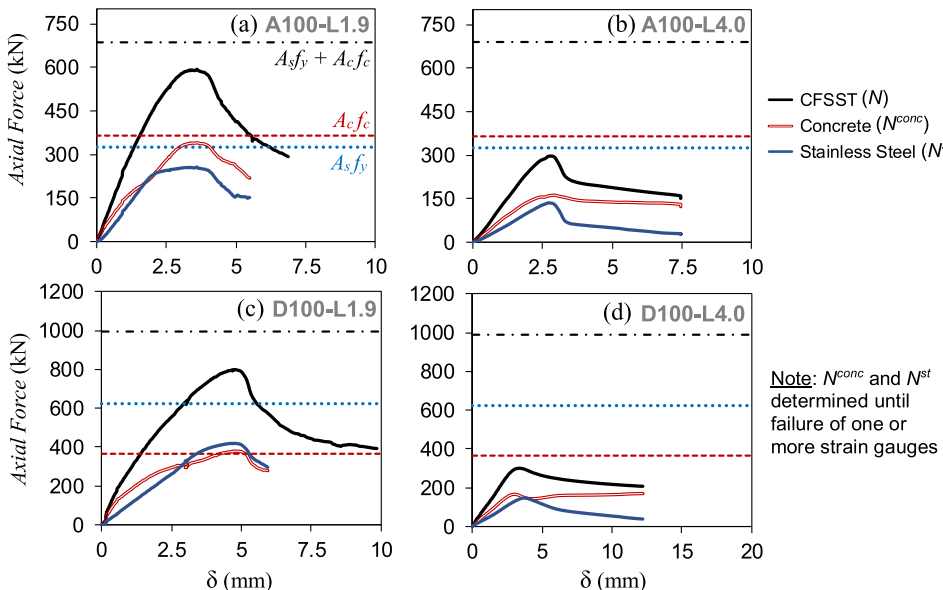


Fig. 14. Test results for long CFSST columns under compression.

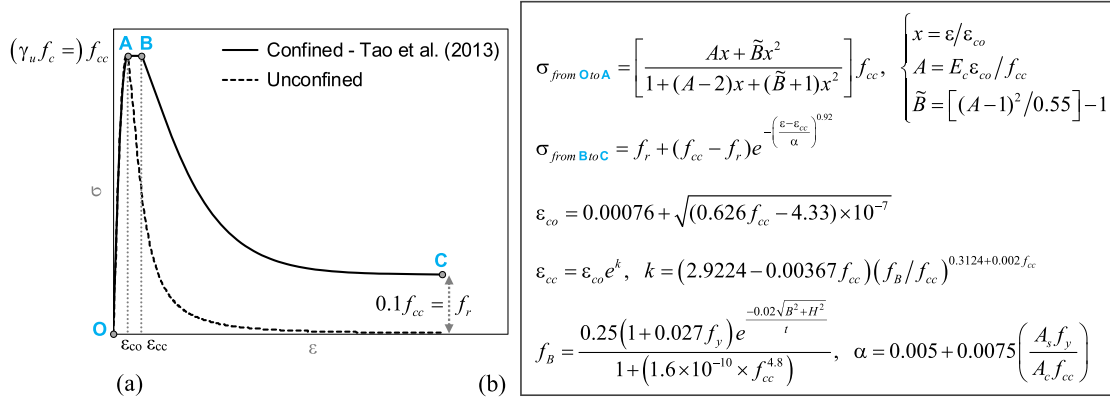


Fig. 15. Slightly modified concrete model of Tao et al. [63] used in the numerical simulations ( $B$  and  $H$  are the external width and depth of the box section respectively).

the biaxial to the uniaxial compressive strength ( $f_{bia}/f_{uni}$ ), and the second stress invariant ratio ( $K_c$ ) were selected as 0.1,  $40^\circ$ ,  $1.5(f_{cc})^{-0.075}$ , and  $5.5/[5 + 2(f_{cc})^{0.075}]$ , respectively. The only modification considered in the present study compared to the original concrete model of Tao et al. [63] was the use of  $f_{cc}$  instead of  $f_c$  (which is typically selected equal to the concrete cylinder strength) in the formulation. As mentioned in Section 4.2 and elaborated further in Section 6.1, test results on larger CFSSTs suggested the possible role of the size effect in lowering the concrete strength. Considering that the CDP model cannot directly capture the effect of the member size on the concrete strength, it was decided to conservatively use  $f_{cc} = \gamma_u f_c$  in the material formulation where  $\gamma_u$  is a size effect reduction factor between 0.85 and 1.0. The formula for  $\gamma_u$  as well as a detailed discussion on the size effect are presented in Section 6.1.1 and not repeated here for brevity.

The tensile behaviour of concrete was assumed to be linear until the stress level of  $0.1f_{cc}$ , followed by a linear descending branch up to a cracking displacement of  $2G_f/0.1f_{cc}$ . The fracture energy can be taken as [68]:

$$G_f [\text{in N/m}] = \begin{cases} \left( 0.0469d_{\max}^2 - 0.5d_{\max} + 26 \right) \left( \frac{f_{cc}}{10} \right)^{0.7} & \text{if } f_{cc} \leq 80 \text{ MPa} \\ \left( 0.0469d_{\max}^2 - 0.5d_{\max} + 26 \right) 4.30 & \text{if } f_{cc} > 80 \text{ MPa} \end{cases} \quad (5)$$

where  $d_{\max}$  is the maximum aggregate size, which was equal to 10 mm for the concrete used in the experiments.

### 5.1.3. Imperfections and residual stresses

Residual stresses were included in the models using the approach proposed in the comprehensive study of Yuan et al. [69] on fabricated

stainless steel sections. This is illustrated in Fig. 16. In addition, geometrical imperfections were also considered in the simulations. For short columns and beams, local imperfections were introduced based on the results of eigenvalue analysis. The magnitude of local imperfections was set to  $b/500$  based on the measurements of Section 3.3. For long columns, on the other hand, both local and global imperfections were incorporated by superimposing different mode shapes obtained from eigenvalue analysis. For the verification, the magnitude of global imperfections was selected as the total imperfection ( $\omega_g + e_{load}$ ) discussed in Section 4.5 and summarised in Table 3. A similar approach can be found in the studies of He et al. [58] and Ban et al. [70]. On the other hand, for comparison of the results with codified column curves, a global imperfection magnitude of  $L/1000$  was used in the parametric study [58,70,71].

#### 5.1.4. Contact and boundary conditions

A nodal adjustment technique was used in ABAQUS to create matching geometries between the outer surface of the concrete core and the inner surface of the stainless steel section. In all models, a surface-to-surface interaction was also introduced at the interface. A hard contact condition prevented the penetration of the surfaces in the normal direction but allowed for their separation. On the other hand, as discussed by Han et al. [65] and Kazemzadeh Azad and Uy [66], the shear stress in the tangential direction could increase until it reached the shear stress limit ( $\tau_{cr}$ ); i.e. the onset of relative slip. According to Han et al. [65],  $\tau_{cr}$  could be defined in the following general form:

$$\tau_{cr} = \mu \sigma_n \geq \tau_b \quad (6)$$

where  $\mu$  is the coefficient of friction,  $\sigma_n$  is the contact or confinement pressure at the interface, and  $\tau_b$  is the average surface bond stress which could be estimated as follows [37,72]:

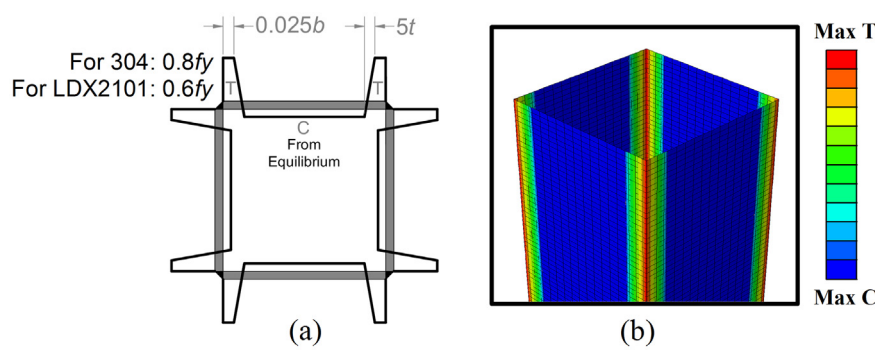


Fig. 16. (a) The residual stress pattern considered in the simulations based on Yuan et al. [69], and (b) its application in a numerical model.

$$\tau_b = \frac{2100t}{(b+2t)^2} \leq 0.7 \text{ [MPa]} \quad (7)$$

As discussed thoroughly by Kazemzadeh Azad and Uy [66], a cohesive model could be employed to include the effect of the average surface bond stress in numerical simulations. However, preliminary analyses suggested that including such a cohesive model resulted in more convergence issues without notable improvements in the accuracy of the results. Consequently, the contact behaviour in the tangential direction was defined as a Coulomb friction model where the shear stress was effectively limited to  $\tau_{cr}$  ( $= \mu\sigma_n$ ), with  $\mu$  set to 0.25 based on the recommendation of Ellobody and Young [26] and Tao et al. [29] for CFSSTs.

The boundary conditions for each model were selected based on the details of the corresponding test setup. For short columns under axial compression, all degrees of freedom were restrained at both column ends, except the vertical displacement at the top end which was used to exert axial shortening to the specimen in a displacement-controlled scheme. For short columns under eccentric loading as well as long columns, the nodes at each column end were constrained to a reference point which was used to apply the boundary conditions. At the bottom reference point, displacements and out-of-plane rotations were restrained, whereas at the top reference point the same boundary conditions were applied except that the vertical displacement was active and used for the load application. In the case of beams, nodes located along the centreline of the roller support were restrained against vertical displacement, whereas those located along the centreline of the pin support were restrained against both vertical and horizontal displacements. Loading was applied as downward displacement along the centrelines of the loading cylinders (Fig. 6b).

## 5.2. Verification

All the tested specimens were modelled based on the details outlined in the previous section in order to verify the accuracy of the FE modelling approach. Comparison of the FE and test results is shown in Fig. 17 where the obtained load (or moment)-deflection curves are compared. In general, FE models were found to have a reasonable

accuracy. The main characteristics of the response, such as the initial stiffness and ultimate capacity, were captured well by the simulations. The components of the total load (or moment) carried by the stainless steel section and concrete infill in the FE models are also compared with those obtained from the tests in Fig. 17. A relatively good match can be observed between the results which further substantiated the applicability of the approach outlined in Section 4.1.

The typical failure modes observed in the FE analyses are depicted in Fig. 18 along with the equivalent plastic strain (PEEQ [62]) contours. As it is seen, the failure modes obtained in the simulations closely resembled those observed in the experimental programme (Fig. 9) in terms of the local and global buckling modes as well as the plastic deformations.

The ultimate axial force ( $N_u^{FE}$ ) and bending moment ( $M_u^{FE}$ ) obtained from the FE analysis are summarised in Table 4 and compared against the test data. The tabulated results suggested that the FE models were capable of accurately predicting the axial and flexural capacities of the tested specimens for both the stainless steel grades and the considered loading schemes.

## 5.3. Parametric study

The verification of the FE modelling approach was followed by a comprehensive parametric study comprising over 200 three-dimensional nonlinear finite element simulations. The main aim was to investigate other geometrical and material properties in order to substantiate the results and to develop design procedures for CFSST members.

An important objective set at the initiation of the parametric study was to design the study such that it would cover an exhaustive range of CFSST sections. Owing to the wide array of geometrical and material combinations that can be used for these members, a special approach, referred to hereafter as the *practical design space*, was considered in the present study to have a manageable number of analyses. The approach is explained next.

Previous studies on concrete-filled tubes have demonstrated that the *section capacity* of a CFT is predominantly affected by two parameters [13,73–77]: the plate slenderness ( $\lambda_e$ ) and the confinement factor ( $\xi$ ). The plate slenderness  $\lambda_e$  shows the propensity of the stainless

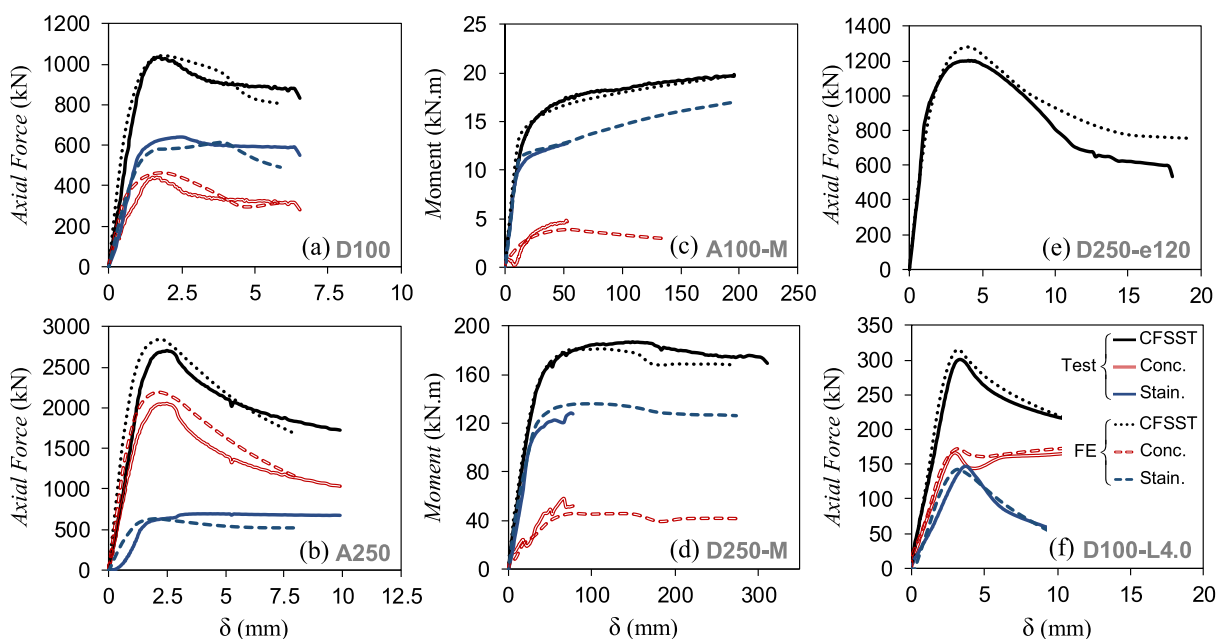


Fig. 17. Comparison of test and FE analysis results for representative specimens.

steel section of a CFSST to local buckling. The concept of the confinement factor ( $\xi$ ), on the other hand, was first introduced by Han et al. [78] as a convenient measure for quantifying the extent of the composite action that takes place between the concrete core and the outer tube in a CFT column. The benefits of using this concept were later illustrated further in the subsequent studies of Han et al. [65,75]. Higher  $\xi$  values typically represent the application of a higher confining pressure from the outer tube to the concrete core, which in turn, can increase the compressive strength of the concrete. Such an increase is also expected in the ductility of the concrete infill [18]. These enhancements were also observed in the tests of the present study. As discussed in Section 4.2 and shown in Fig. 8a,c, specimens A100 and D100 were both relatively compact, however, the confinement factor for the latter was almost twice that of the former specimen. In line with this, as it can be seen in the figure, the concrete core in D100 was able to carry axial loads notably higher than its nominal compressive strength and exhibited great strength retention. Han et al. [78] also proposed that the response type of a concrete-filled column can be categorised based on its corresponding  $\xi$ . It was demonstrated that if the value of  $\xi$  for a column was above a certain threshold, a strain-hardening type response was observed under axial compression. On the other hand, columns with lower  $\xi$  values exhibited strength degradation after reaching their ultimate capacity. As elaborated further in Section 6.3, recent studies by researchers such as Choi et al. [77] and Lai et al. [73] showed that the concept of the confinement factor can also be used to demonstrate whether the behaviour of a CFT member under combined compression and bending is more inclined towards that of a bare steel section (high  $\xi$ ) or a reinforced concrete section (low  $\xi$ ). It was demonstrated that the shape of the axial-flexural ( $N$ - $M$ ) interaction curve became rounder for lower  $\xi$  values and changed to a more bilinear form for higher  $\xi$  values.

An important aspect of the plate slenderness and the confinement factor is that the material properties are also accounted for in these parameters. As discussed in Section 3.1, the plate slenderness used in the present study is  $\lambda_e = (b/t)\sqrt{f_y/250}$  as per AS/NZS 2327 [34]. On the

other hand, the confinement factor is typically defined as the ratio between the compressive strengths of the outer tube and the concrete core. The confinement factor proposed originally by Han et al. [78] was  $\bar{\xi} = A_s f_y / A_c f_{ck}$  (with  $f_{ck}$  in the denominator) where the characteristic (5% fractile) concrete strength,  $f_{ck}$ , could be estimated as  $0.67 f_{cu}$ . Furthermore,  $f_{cu}$  is typically referred to as the cubic concrete strength in the literature [65,75,78], although strictly speaking it is the characteristic cubic concrete strength as per the Chinese concrete code GB 50010 [79]. It is important to emphasise that the definition of the characteristic concrete strength,  $f_{ck}$ , is not necessarily consistent across different standards. For instance, AS 3600 [80] provides a table which correlates the mean value of cylinder compressive strengths to the characteristic strength. Eurocode 2 [81], on the other hand, estimates  $f_{ck}$  as the mean value of cylinder compressive strengths minus 8 MPa. A number of recent studies have used a slightly different definition for the confinement factor in their investigations, i.e.  $\xi = A_s f_y / A_c f_c$ , where the cylindrical concrete strength ( $f_c$ ) was used in the denominator [63,73,82,83]. In the present study, this definition ( $\xi = A_s f_y / A_c f_c$ ) was considered in order to use a single, consistent measure of the concrete strength (i.e.  $f_c$ , determined herein from concrete cylinder tests) for investigating the experimental data, conducting FE simulations, and developing design formulae. It should be emphasised that, using  $\xi$  or  $\bar{\xi}$  will lead to slightly different confinement factors, and therefore, it is important to clarify which definition is used in any investigation.

Based on the above discussions, one can characterise the sectional behaviour of a CFSST simply by its corresponding coordinates in a  $\lambda_e$  -  $\xi$  coordinate system. Next, it is essential to determine a space in the  $\lambda_e$  -  $\xi$  coordinate system which a CFSST section can practically lie within. To find this *practical design space*, first the relation between  $\lambda_e$  and  $\xi$  was established as follows:

$$\lambda_e = \frac{b}{t} \sqrt{\frac{f_y}{250}} \rightarrow b = \lambda_e t \sqrt{\frac{250}{f_y}} \quad (8)$$

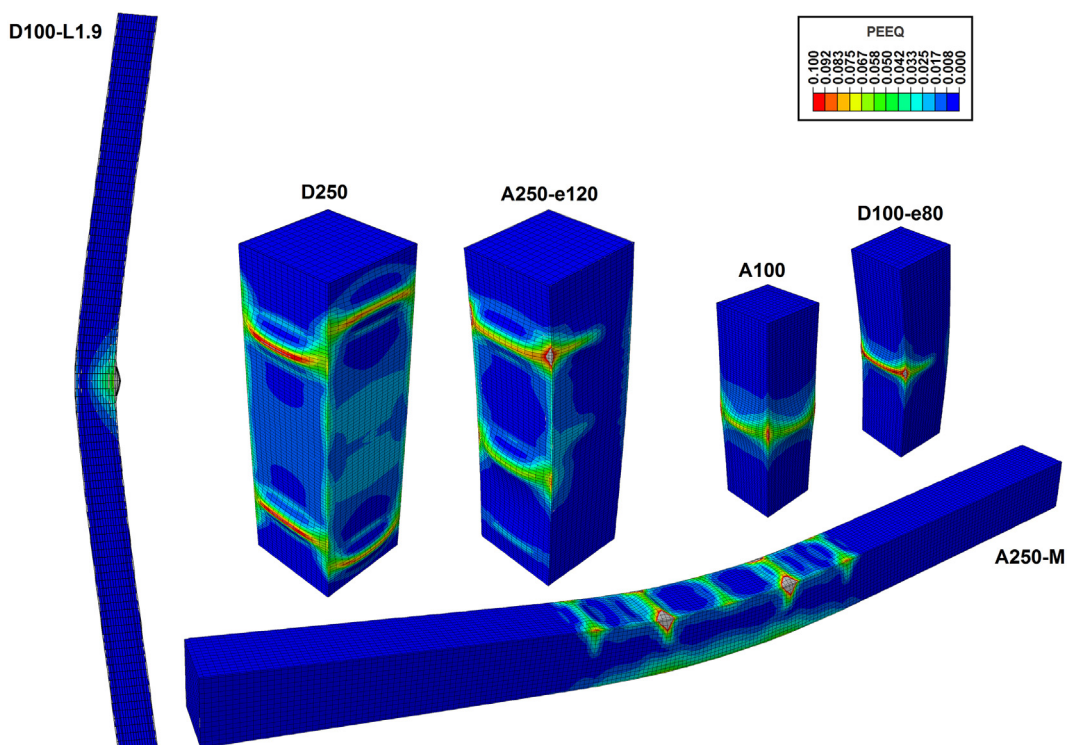


Fig. 18. Typical failure modes observed in the FE analyses.

$$\xi = \frac{A_s f_y}{A_c f_c} = \frac{4bt f_y}{b^2 f_c} \xrightarrow{b \text{ from Eq.(8)}} \xi = \frac{1}{\lambda_e} \cdot \frac{4(f_y)^{1.5}}{\sqrt{250} f_c} \quad (9)$$

Eq. (9) implies that, one can simply select a practical range for  $f_y$ ,  $f_c$ , and  $\lambda_e$ , and find the full possible range of  $\xi$  values. This was carried out in the present study considering  $25 \leq f_c \leq 70$  MPa,  $250 \leq f_y \leq 600$  MPa, and  $25 \leq \lambda_e \leq 160$  which cover a very wide range of CFSSTs. Please note the concrete-filled tubes with a plate slenderness of less than 25 could be utilised in practice. However, these are very compact sections which, according to previous tests [18], exhibit very high levels of strain hardening, that is traditionally ignored in international standards, and results in conservatism designs. Consequently, more focus was put on sections with higher slenderness values. It is also worth noting that the considered upper slenderness limit of 160 is even higher than the maximum allowed by AISC 360–16 [37] which currently is the only standard which provides complete design recommendations for carbon steel CFSTs with slender sections. Based on these ranges and using Eq. (9), the limits for the maximum and minimum  $\xi$  values were determined and plotted in Fig. 19a. Inside these lines can be considered the practical design space for square CFSSTs with  $f_c \leq 70$  MPa and  $f_y \leq 600$  MPa.

In order to investigate the effect of web buckling on the behaviour of CFSST beams, it was deemed necessary to also include a series of models with rectangular sections in the parametric study. Consequently, Eq. (9) was re-established for rectangular sections, as follows, and the corresponding practical design space was determined and plotted accordingly in Fig. 19b:

$$\xi = \frac{\lambda_e^f + \lambda_e^w}{\lambda_e^f \lambda_e^w} \cdot \frac{2(f_y)^{1.5}}{\sqrt{250} f_c} \quad (10)$$

where  $\lambda_e^f$  and  $\lambda_e^w$  are the plate slenderness values of the flange and web, respectively. Eq. (10) simplifies to Eq. (9) when  $\lambda_e^f = \lambda_e^w = \lambda_e$  (i.e. for square sections). In Fig. 19b, the upper limit for the plate slenderness was increased from 160 to 200 to include very deep rectangular CFSST beams as well.

After establishing the practical design spaces, a very wide range of section geometries and material properties were considered to cover this space as much as possible. As it can be seen in Fig. 19, the parametric study models were able to achieve this goal, albeit at the expense of a significant number of simulations. Details of the parametric study

models can be found in Table 5 for square CFSST columns, and in Table 6 for square/rectangular CFSST beams. According to the tables, both austenitic and duplex, compact and slender sections were considered.

As summarised in Table 5, several columns were analysed under compression, as well as combined compression and bending. For the combined loading cases, each column was simulated under pure compression, pure bending, and three axial load ratios, namely 10%, 30%, and 50% of its obtained axial capacity. Furthermore, a series of long columns with compact and slender sections were included in the parametric study with relative slenderness ( $\lambda$ ) values ranging from 0.5 to 2.3. Based on Table 6, a wide range of square and rectangular CFSST beams with compact and slender flanges were considered in the parametric study. It should be noted that both  $\lambda_e^f$  and  $\lambda_e^w$  are independent variables in Eq. (10), however, considering the limitations of 2D plots, in Fig. 19b,  $\lambda_e^w$  is shown in the x-axis and colour-coding is used to distinguish between models with compact flanges ( $\lambda_e^f \leq 50$ ) and those with slender flanges ( $\lambda_e^f > 50$ ). The results obtained from the experiments are combined with those of the parametric study in the next section to propose recommendations for the design of CFSST members.

## 6. Discussion of results and design recommendations

### 6.1. CFSST section capacity: axial compression

#### 6.1.1. Design recommendations considering local buckling and size effect

The axial capacity of a CFSST section can be accurately predicted if the axial capacities of its stainless steel and concrete components are correctly predicted. Consequently, the approach considered in the experiments and analyses of the present study was to apply the loading to the entire CFSST column but trace the behaviour of the stainless steel section and the concrete infill separately. This provided a much clearer understanding of the response compared to focusing solely on the total resisted load.

The experiments of the present study on compact and slender CFSSTs (Fig. 8) clearly demonstrated that the axial force resisted by the stainless steel section of a CFSST will reduce drastically if premature local buckling occurs. Consequently, the plate slenderness needs to be accounted for in the design of these sections. To this end, as discussed in Section 4.2 and illustrated in Fig. 8c, the component of the load resisted by the stainless steel section when the entire CFSST reached its ultimate load (i.e.  $N_u^{st}$ ) was extracted from the test results (Table 4)

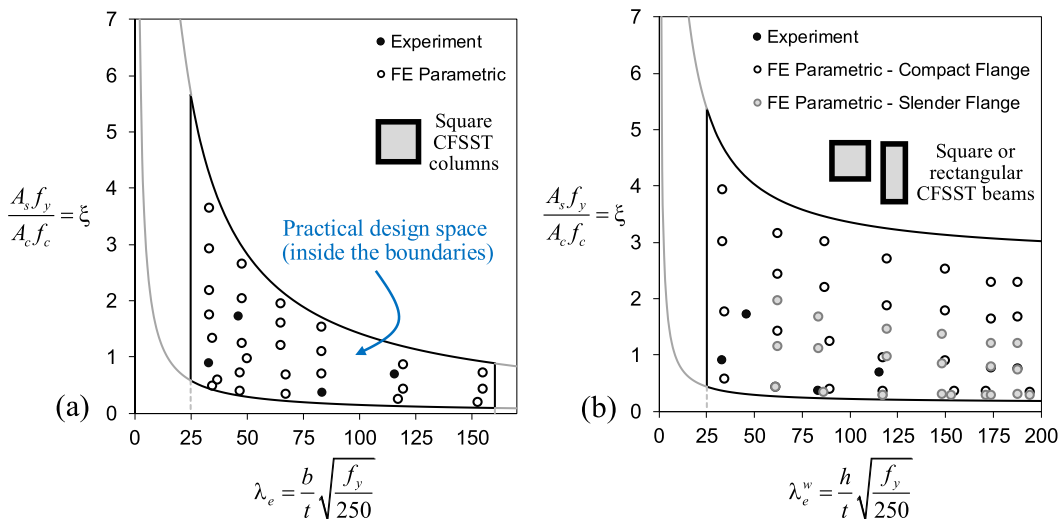


**Fig. 19.** Practical design space for CFSSTs with  $f_c \leq 70$  MPa and  $f_y \leq 600$  MPa, and the selected parametric study models for (a) square CFSST columns and (b) square or rectangular CFSST beams.

**Table 5**

Details of the parametric study for square CFSST columns.

b (mm)	t (mm)	$f_c$ (MPa)	$f_y$ (MPa)*	$\lambda_e$	$\xi$	$\lambda$	Section Type**	Loading Type(s)***		
								$N_{short}$	$N + M^{****}$	$N_{long}$
100	2.2	32	266	47	0.73	–	C	●		
100	2.2	59	266	47	0.40	0.5, 2.0	C	●	●	●
100	3.0	24	266	34	1.33	–	C	●		
100	3.0	66	266	34	0.48	–	C	●		
100	3.0	49	511	48	1.25	–	C	●		
100	3.0	23	511	48	2.67	1.0, 2.3	C	●	●	●
100	3.0	30	511	48	2.04	–	C	●		
100	4.3	50	511	33	1.76	–	C	●		
100	4.3	24	511	33	3.66	1, 1.5	C	●	●	●
100	4.3	30	511	33	2.93	–	C	●		
100	4.3	40	511	33	2.20	0.5, 2.0	C	●		
195	3.0	24	266	67	0.68	–	S	●		
195	3.0	48	266	67	0.34	0.5, 1.2	S	●	●	●
195	4.3	28	511	65	1.61	–	S	●		
195	4.3	37	511	65	1.22	–	S	●		
195	4.3	23	511	65	1.96	0.9, 1.8	S	●	●	●
250	2.2	38	266	117	0.25	0.8, 1.1	S	●	●	●
250	3.0	28	511	119	0.88	0.6, 1.3	S	●	●	●
250	3.0	56	511	119	0.44	–	S	●		
250	4.3	23	511	83	1.53	–	S	●	●	
250	4.3	32	511	83	1.10	–	S	●	●	
250	4.3	50	511	83	0.70	–	S	●		
325	2.2	37	266	152	0.19	0.7, 1.8	S	●	●	●
325	3.0	26	511	155	0.73	1.1, 1.5	S	●	●	●
325	3.0	43	511	155	0.44	–	S	●	●	
350	10.0	60	511	50	0.97	–	C	●		
250	7.0	50	266	37	0.60	–	C	●		

\* Specimens with  $f_y = 266$  MPa are austenitic and those with  $f_y = 511$  MPa are lean duplex.

\*\* In this table C: compact; S: slender.

\*\*\*  $N_{short}$ : short column under axial force;  $N + M$ : short column under combined loading;  $N_{long}$ : long column under axial force.\*\*\*\* For the case of combined loading ( $N + M$ ), each model was run considering four axial load ratios (0, 0.1, 0.3, 0.5).**Table 6**Details of the parametric study for square and rectangular CFSST beams (all dimensions in mm and stresses in MPa;  $h$ : internal web height).

b	h	t	$f_c$	$f_y^*$	$\lambda_e^f$	$\lambda_e^w$	$\xi$	Flange Type**	b	h	t	$f_c$	$f_y$	$\lambda_e^f$	$\lambda_e^w$	$\xi$	Flange Type
55	130	2.2	70	266	26	61	0.43	C	130	130	2.2	41	266	61	61	0.44	S
55	250	2.2	27	266	26	117	0.96	C	130	130	3.0	41	511	62	62	1.15	S
55	365	2.2	69	266	26	171	0.35	C	130	130	3.0	24	511	62	62	1.97	S
55	130	3.0	25	511	26	62	3.17	C	180	250	2.2	38	266	84	117	0.29	S
55	250	3.0	36	511	26	119	1.89	C	180	250	3.0	20	511	86	119	1.46	S
55	250	3.0	25	511	26	119	2.72	C	195	365	2.2	31	266	91	171	0.30	S
55	365	3.0	28	511	26	174	2.29	C	195	250	3.0	43	266	67	86	0.34	S
75	100	3.0	64	266	26	34	0.58	C	195	365	3.0	20	511	93	174	1.21	S
75	100	3.0	21	266	26	34	1.77	C	195	250	4.3	36	511	65	83	1.11	S
75	260	3.0	22	266	26	89	1.25	C	250	250	2.2	32	266	117	117	0.29	S
75	565	3.0	70	266	26	194	0.34	C	250	445	3.0	34	266	86	153	0.29	S
75	100	4.3	34	511	25	33	3.02	C	250	250	3.0	25	511	119	119	0.98	S
75	100	4.3	26	511	25	33	3.94	C	250	250	4.3	21	511	83	83	1.67	S
75	260	4.3	25	511	25	86	3.02	C	250	445	4.3	20	511	83	148	1.37	S
75	450	4.3	38	511	25	150	1.80	C	250	565	4.3	21	511	83	188	1.21	S
75	450	4.3	27	511	25	150	2.53	C	365	565	3.0	25	266	125	194	0.29	S
75	565	4.3	29	511	25	188	2.29	C	365	365	3.0	57	511	174	174	0.29	S
110	250	2.2	43	266	52	117	0.36	C	365	365	3.0	21	511	174	174	0.80	S
110	130	3.0	36	511	52	62	1.43	C	445	445	4.3	65	511	148	148	0.30	S
110	130	3.0	21	511	52	62	2.45	C	445	445	4.3	23	511	148	148	0.86	S
110	365	3.0	47	511	52	174	0.77	C	565	565	4.3	51	511	188	188	0.31	S
110	365	3.0	22	511	52	174	1.65	C	565	565	4.3	21	511	188	188	0.74	S
150	260	3.0	43	266	52	89	0.39	C									
150	450	3.0	40	266	52	155	0.35	C									
150	260	4.3	21	511	50	86	2.20	C									
150	450	4.3	43	511	50	150	0.91	C									
150	565	4.3	49	511	50	188	0.76	C									
150	565	4.3	22	511	50	188	1.69	C									

\* Specimens with  $f_y = 266$  MPa are austenitic and those with  $f_y = 511$  MPa are lean duplex.

\*\* In this table C: compact; S: slender.

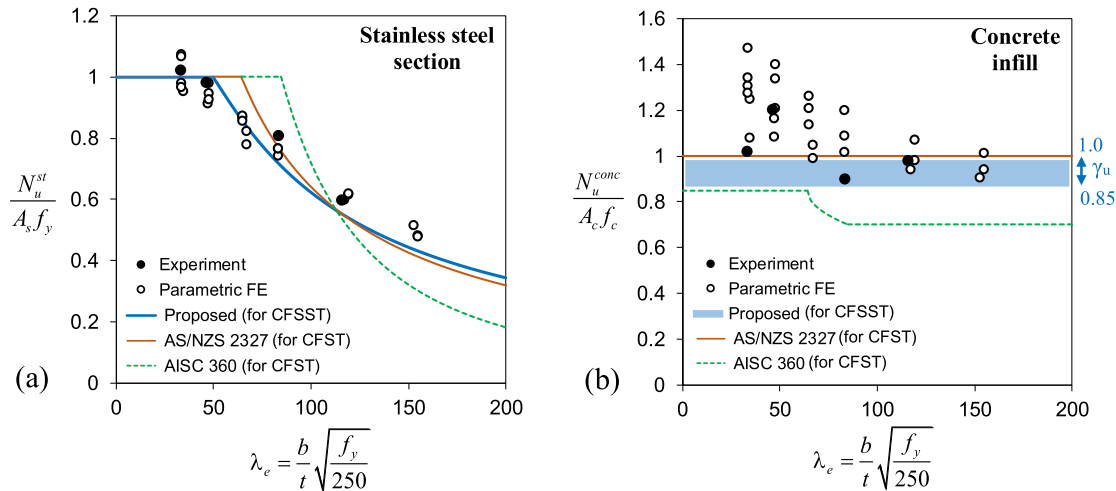


Fig. 20. Forces resisted by (a) the stainless steel section and (b) the concrete infill in short CFSSTs under compression.

as well as the parametric study models and normalised with respect to the yield load of the stainless steel section ( $A_s f_y$ ) in Fig. 20a. It is evident from the figure that slender stainless steel sections are unable to attain their yield load. In order to capture this effect in the design of CFSSTs, the approach proposed by Uy [13] for slender carbon steel CSFTs was considered herein, however, using the *effective width* formula developed recently by Kazemzadeh Azad et al. [24,25] specifically for box CFSSTs. In this approach, the width ( $b$ ) of the CFSST walls with  $\lambda_e > 50$  is simply reduced to  $b_e$ , as follows, for determining the stainless steel component of the axial capacity:

$$\frac{b_e}{b} = \begin{cases} 1.0 & \text{if } \lambda_e \leq 50 \\ \left(1.49 \times \frac{50}{\lambda_e}\right) \left[1 - 0.22 \left(1.49 \times \frac{50}{\lambda_e}\right)\right] & \text{if } \lambda_e > 50 \end{cases} \quad (11)$$

where  $b_e$  is the effective width of each CFSST wall that is dependent on its plate slenderness  $\lambda_e$ , and the value of 50 is the axial slenderness limit proposed by the authors in [24,25] for box CFSSTs. It is worth mentioning that Kazemzadeh Azad et al. [24,25] also proposed a simplified but more conservative equation (i.e.  $b_e/b = 50/\lambda_e$ ) which could also be used. Comparisons made considering the two formulae (not reported here for brevity) suggested that Eq. (11) correlated better with the data while the simplified formula was more conservative. Consequently, Eq. (11) was used hereafter. As it can be seen in Fig. 20a, the proposed approach predicts the experimental and numerical results with a good accuracy. The slight overestimation in the vicinity of the slenderness limit ( $\lambda_e = 50$ ) was deemed acceptable owing to its small magnitude (less than 8%) as well as the high concrete confinement effect typically observed in this region (discussed next) which easily counter-balanced it.

A similar procedure was carried out for the ultimate load resisted by the concrete core. The  $N_u^{\text{conc}}/A_c f_c$  values summarised in Fig. 20b revealed that the concrete core was notably less sensitive to the slenderness of the section and could reach to strengths close to its plastic capacity ( $A_c f_c$ ) even if the outer section was very slender. A significant overstrength was observed particularly for compact sections which provided confinement to the concrete core. Nevertheless, an experimental observation suggested a slight reduction factor to be included. As mentioned in Section 4.2, tests on the 250 mm-wide CFSSTs suggested a possible influence of the size effect on the concrete strength. This can also be observed from the experimental results in Fig. 20b.

The effect of size on the strength of the concrete infill of a CFT is a difficult phenomenon to be investigated. The reason is that many factors such as the confinement, curing conditions, inherent variability in the concrete strength, and section size can affect the strength of the concrete

infill, and distinguishing them from one another based on the test results is not straightforward. More importantly, there is a significant lack of test data in this regard, since the majority of the previous tests have not separated the loads carried by the outer section and the concrete infill. Furthermore, the size effect cannot be captured directly by conventional FE analysis, and it can only be manually introduced in the form of a reduced concrete strength as outlined in Section 5.1.2 (though more advanced numerical methods are also available). This prevented conducting a direct numerical investigation into the issue.

Through the years many studies, including Blanks and McNamara [84], Bažant [85], Kim et al. [86], and Aslani [87], have confirmed that size has indeed an effect on the strength of plain concrete cylinders. However, for the concrete core of a CFT, different perspectives can be found in the literature. For instance, a recent study by Hu et al. [53] could not identify notable size effect based on a series of tests on box carbon steel CFSTs. This was attributed to the effect of the confinement on reducing the size effect. It should however be noted that the tests of Hu et al. [53] were on compact or slightly-slender CFSTs. Postprocessing of the data of the tests conducted by Uy [32] and later by Mursi and Uy [88] on CFSTs with small and relatively large sections suggested that a reduction factor of 0.85 for the compressive strength of concrete is necessary only for some of the tests with slender sections (but not all the slender specimens). This was attributed to a combination of the confinement effect and improved curing conditions for CFSTs. American design codes have traditionally used a reduction factor of 0.85 for the concrete strength in CFSTs which, according to the pioneering study of Schneider [89], is mainly to account for the size effect. Japanese studies, such as Sakino et al. [12], Yamamoto et al. [90], and Fujimoto et al. [91], have also generally accounted for the size effect. More recent studies by Chinese researchers have also concluded that the size effect is influential in the strength of CFTs [92].

Consequently, in the present study, it was decided to include a reduction factor to account for the size effect. The reasons for this were: (i) while there is no consensus, more studies in the literature appear to be leaning towards considering the size effect in the CFT design; (ii) the test results of the present study and their comparison with a series of supplementary FE analyses also suggested a possible influence of the size effect; and (iii) while the tests reported herein provided some insight on the behaviour of large fabricated CFSSTs, considering the general lack of tests on such specimens, it was advisable to conservatively consider the size effect; this was particularly important considering that CFSSTs are primarily intended for use in large infrastructure projects.

As mentioned earlier, the size effect in CFTs is a rather difficult issue to be investigated. While the experiments of the present paper provided

some insight, it should be emphasised that a comprehensive study on the size effect would require many more specifically-designed specimens to be tested. For instance, a more direct investigation on the size effect could be conducted by comparing the test results for specimens with the same width, but different thicknesses; or by comparing the test results for specimens of different widths, but with the same confinement factor ( $\xi$ ). While the limitations of the testing programme, including the main research objectives, total number of specimens, available resources, and time constraints, did not allow for such a direct comparison to be carried out herein, based on the preceding discussions, it was advisable to conservatively consider the size effect in the design of CFSSTs. To this end, the following reduction factor was considered:

$$0.85 \leq \gamma_u = \begin{cases} 1.97D_c^{-0.135} & \text{if } f_c \text{ is determined from 150 mm cylinders} \\ 1.85D_c^{-0.135} & \text{if } f_c \text{ is determined from 100 mm cylinders} \end{cases} \leq 1.0 \quad (12)$$

where  $\gamma_u$  is the size effect reduction factor and  $D_c$  (in mm) is the characteristic dimension of the concrete core which can be taken as  $2B/\sqrt{\pi}$  for box section sections [91], where  $B = b + 2t$ . The main equation was originally recommended by Sakino et al. [12] and later revised by Liang [93]. It was very slightly modified herein to provide a  $\gamma_u$  of unity for cylinders with a diameter of 150 mm which was used in the material tests of Section 3.2. The  $\gamma_u$  factor can take values between 0.85 and 1.0 based on the section size, and its range is illustrated in Fig. 20b with a blue shaded area. For instance, a  $\gamma_u$  of 0.9 indicates that the compressive strength obtained from a cylinder test ( $f_c$ ) needs to be reduced by 10% to account for the size effect.

Considering the contributions of the stainless steel outer section and the concrete infill, the following design formula can be recommended for predicting the axial capacity of a compact or slender CFSST section:

$$N_{prop} = \begin{cases} A_s f_y + \gamma_u A_c f_c & \text{if } \lambda_e \leq 50 \\ A_e f_y + \gamma_u A_c f_c & \text{if } 50 < \lambda_e \leq 140 \end{cases} \quad (13)$$

where  $\lambda_e = (b/t)\sqrt{f_y/250}$  and  $\gamma_u$  is found from Eq. (12). In addition,  $A_e$  (for the slender case) is the effective area of the stainless steel section determined as the sum of the effective widths of the CFSST walls times their thickness (i.e.  $\sum b_e t$ ). The effective width of each wall ( $b_e$ ), on the other hand, can be determined using Eq. (11). An upper limit of 140 was considered for the plate slenderness, following AISC 360 [37], due to the lack of research in this range and construction-related issues with such extremely slender sections.

#### 6.1.2. Comparison with design codes and other proposed methods

In order to investigate the accuracy and applicability of the proposed formula ( $N_{prop}$ ), the approach is compared with the results obtained from international design standards and methods proposed by others. The effective width formula recommended in the present study (Eq. (11)) is compared in Fig. 20a with the test and FE analysis results along with the effective width formulae currently in use by the Australian [34] and American [37] design specifications for carbon steel CFSTs. It should be noted that Eurocode 4 [60] only allows compact sections with  $\lambda_e \leq 50$  to be utilised. In AS/NZS 2327 [34], the reduction in steel strength due to local buckling starts at  $\lambda_e = 64$ , which is higher than the slenderness limit of 50 considered herein. Therefore, slight overestimations of the local buckling strength are observed. The AISC 360–16 [37] curve starts to descend even later (at  $\lambda_e = 85$ ), with a steeper trend, which leads to significant overestimations in the early parts of the curve and notable underestimations towards higher slenderness values. It should however be emphasised that these codes are intended for CFSTs, and not CFSSTs, and the results clearly demonstrated the need for modifications so that these approaches can be safely applied to CFSSTs.

In terms of the concrete component of the axial capacity, as shown in Fig. 20b, the Australian standard [34] does not consider any reductions

(i.e. uses  $A_c f_c$ ). However, it should be noted that, based on Clause 4.1.1.2 of AS/NZS 2327 [34], the maximum allowed slenderness for a concrete-filled column is 85. Based on the figure, the concrete core in some of the specimens failed to achieve this full plastic capacity due to low confinement and possible size effect, as discussed in the previous section. In contrast, AISC 360–16 [37] uses a more conservative approach where the concrete capacity is capped at  $0.85A_c f_c$  for compact sections until  $\lambda_e = 64$ , followed by a nonlinear transition range (from  $\lambda_e = 64$  to 85) which reduces the concrete capacity further down to  $0.7A_c f_c$ . While the use of the reduction factor of 0.85 appears to be reasonable considering the possible confinement- and size effect-related issues, the data presented in Fig. 20b suggest that a further reduction to 0.7 appears to be too conservative. This was also highlighted in Kazemzadeh Azad et al. [24]. This further reduction was recommended in a study by Lai et al. [74], however, in a more recent study by Lai and Varma [51] on high-strength CFSTs the factor was suggested to be increased back to 0.85 provided that a better prediction of the behaviour of the steel section is included in the design equation. As shown in Fig. 20b with a blue shaded area, in order to have a reasonable balance between safety and economy of design, the approach recommended in the present study uses a simple variable reduction factor ( $\gamma_u$  from Eq. (12)) to move the concrete capacity between the two limits of  $0.85A_c f_c$  and  $A_c f_c$  depending on the section size.

In order to have a clearer comparison between the different approaches, the ultimate loads obtained from the tests and FE analyses are compared with the predictions of the proposed method (Eq. (13)) as well as those of the specifications in Fig. 21. The figure also contains a compilation of CFSST test results from the literature, considering square specimens with a conventional concrete core,  $f_c < 70$  MPa, and  $\lambda_e > 20$ . The test data was compiled from the experimental results reported previously in the following studies: Young and Elloboddy [16], Lam and Gardner [17], Uy et al. [18], Yang and Ma [20], Lam et al. [19,94], and Liao et al. [21]. For cases where only the cubic concrete strength ( $f_{cu}$ ) was reported in the original reference, the following formula was used to estimate the cylindrical concrete strength ( $f_c$ ) [63,95]:

$$f_c = \left[ 0.76 + 0.2 \log_{10} \left( \frac{f_{cu}}{19.6} \right) \right] f_{cu} \text{ [MPa]} \quad (14)$$

Based on Fig. 21a-d, all methods, including the proposed method, provided rather conservative results when compared with the data for compact sections. The results related to some of the previous tests are highly conservative, mainly owing to the fact that a large number of previous tests have been conducted on very compact, small sections which experience very high strain hardening and confinement effects.

However, when slender sections (i.e.  $\lambda_e > 50$ ) are approached, stark differences are observed in the figure among the methods. The proposed method (Fig. 21a), predicted the ultimate loads safely and with a reasonable accuracy, with only a few unconservative predictions of the previous tests in the literature. A similar trend could be observed in Fig. 21b for AS/NZS 2327 with some unconservative results particularly for moderately slender columns due to considering no reduction factors for the concrete strength and using an effective width concept developed for carbon steel CFSTs.

As noted earlier, Eurocode 4 only allows compact sections with  $\lambda_e \leq 50$  to be utilised. Consequently, as shown in Fig. 21c, the predictions of this code are rather unsafe for CFSSTs with slender sections. This is expected since the code does not account for local buckling in its predictions.

As shown in Fig. 21d, a drastically different trend can be seen for AISC 360, with extremely conservative predictions for slender sections due to the use of the 0.7 reduction factor (discussed earlier) in the concrete strength.

A few methods have also been developed in other studies for predicting the axial capacity of a CFSST sections. Hassanein [27] proposed  $[0.96(A_s f_y + 0.85A_c f_c)]$  whereas Lam et al. [19] recently proposed  $[A_s \sigma_{1,0} + 1.1A_c f_c]$  where  $\sigma_{1,0}$  is the stainless steel strength at 1% strain.

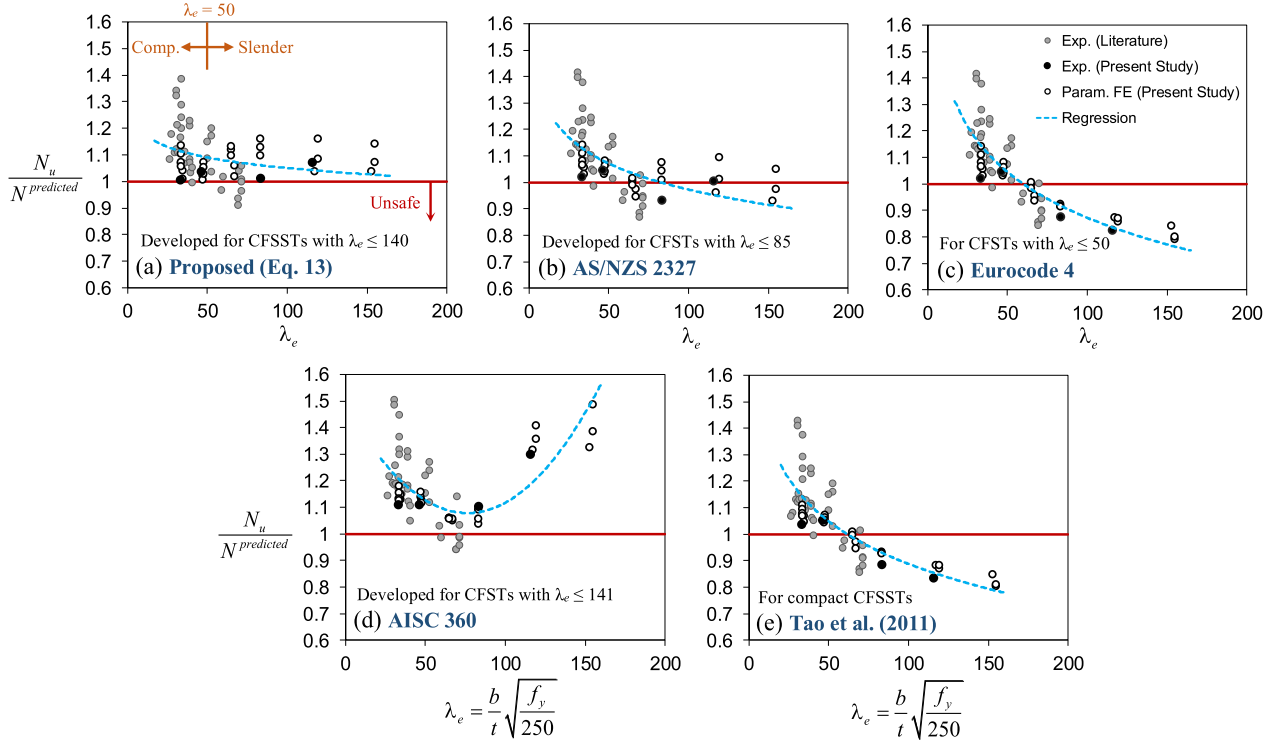


**Fig. 21.** Comparison of the axial capacities predicted by different approaches with the test and FE results.

Based on a series of FE analyses, Tao et al. [29] recommended  $[\bar{k}A_s f_y + A_c f_c]$  with  $\bar{k}$  calibrated as  $[0.946 + 0.021\bar{\xi}]$ . It should be emphasised that  $\bar{\xi}$  ( $= A_s f_y / A_c f_{ck}$ ) is used in the last expression which, as explained

in detail in Section 5.3, is based on the characteristic concrete strength commonly found in Chinese codes and literature [79] (i.e.  $f_{ck} = 0.67 f_{cu}$ ).

The formulae proposed by Hassanein [27], Lam et al. [19], and Tao et al. [29] all appear to be intended mainly for highly compact CFSTs

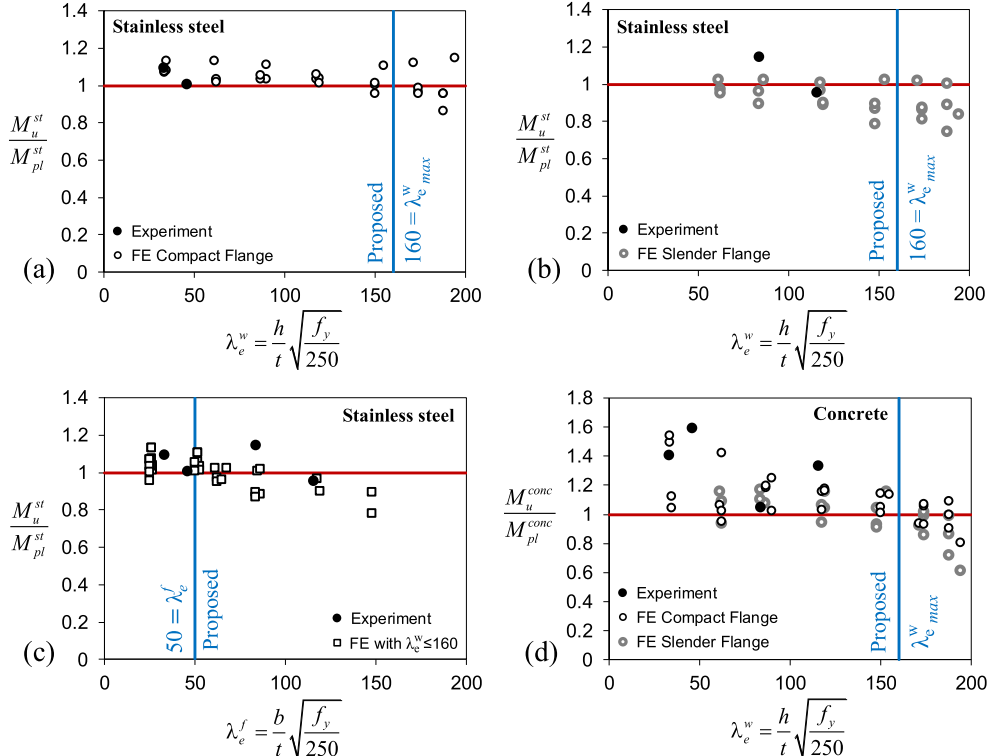


**Fig. 22.** Moments resisted by the stainless steel section and the concrete infill in CFST beams under bending.

as they do not have any parameter related to the plate slenderness which is the key for proper prediction of the local and post-local buckling strength. As an example, the predictions of the formula developed by Tao et al. [29] are compared with the dataset in Fig. 21e, and as expected, the formula was found to be only reliable in the compact region. It should be noted that the value of  $f_{ck}$  ( $= 0.67f_{cu}$ ) needed in Toa et al.'s [29] method was either directly calculated from the  $f_{cu}$  value reported in the original reference or by back-calculating the  $f_{cu}$  value based on the reported  $f_c$  value and using Eq. (14). In essence, to have a fair comparison between the predictions of different approaches, it is necessary to use the correct strength parameters associated with each approach.

A study by Ellobody and Young [26] developed a design procedure for CFSSTs based on the concept of effective area, however, using the effective width relations mainly developed for hollow tubes, as such relations were not available at the time for concrete-filled stainless steel tubes. Application of the Continuous Strength Method [9] to the design of CFSSTs was also investigated by Lam and Gardner [17], however, similar to Ellobody and Young [26], neglecting the beneficial effects of the concrete infill in increasing the local buckling strength of the outer stainless steel section. The method has however the potential to include such effects and could be investigated further in future studies.

## 6.2. CFSST section capacity: Flexural bending

### 6.2.1. Design recommendations including slenderness limits for flexure

A systematic investigation, similar to that of the previous section, was carried out in this section for the case of CFSST beams under pure bending. To this end, in each test or FE analysis, the contributions of the stainless steel section ( $M_{pl}^{st}$ ) and the concrete core ( $M_{pl}^{conc}$ ) to the ultimate moment of the CFSST beam were first determined and then normalised with respect to the corresponding plastic capacities  $M_{pl}^{st}$  and  $M_{pl}^{conc}$  (Fig. 22). It should be emphasised that  $M_{pl}^{st}$  is not equal to the plastic moment capacity of a hollow stainless steel section, and it is rather the share of the stainless steel section when the entire CFSST reaches its plastic state. Please refer to Section 4.3 and Fig. 12a for complete definitions.

One of the main aims of the present study was to define slenderness limits for CFSSTs under flexure based on the results of the experiments and numerical simulations. In line with this, the results corresponding to specimens with a wide range of web slenderness values ( $\lambda_e^w$ ), but all with compact flanges, were first summarised in Fig. 22a. It should be noted that, since the top flange was mainly under uniform compression, a slenderness limit of  $\lambda_e^f = 50$  (similar to that of the walls of CFSSTs under pure compression) was used to categorise compact and slender flanges. This assumption is substantiated later. Results summarised in Fig. 22a revealed an interesting issue. In almost all specimens with compact flanges, the stainless steel section was able to attain  $M_{pl}^{st}$  provided that  $\lambda_e^w$  was kept below 160 (which is extremely slender). This is a very important outcome as it suggests that the web buckling has limited influence on the behaviour of the stainless steel section in a CFSST beam. This is unlike a hollow box section which will exhibit gradual reduction in strength with increasing web slenderness as a result of web buckling. A careful investigation of the results demonstrated that three factors are behind this: (i) in CFSSTs under pure bending, unlike hollow box sections, the presence of the concrete infill shifts the neutral axis higher, resulting in a smaller compression region in the web, reducing the susceptibility to web buckling, (ii) more importantly, the presence of the concrete core increases the local buckling strength of the web by preventing its inward deformations, and (iii) the presence of the concrete core increases the local buckling strength of the flange, which also contributed to the local stability of the web as a connecting element. These three factors provide the opportunity for the web to exhibit its full plastic capacity. Consequently, it was concluded that the web of a CFSST beam can be categorised as compact simply as long as  $\lambda_e^w \leq (\lambda_e^w)_{max} = 160$ . As shown in Fig. 22a, beyond this upper limit, the strength of the stainless steel section started to decrease as a result of web buckling. It should be

emphasised that this is a very high upper limit, and advisable not to be exceeded due to practical issues and lack of experiments in this range [74].

Next, the procedure was repeated for CFSSTs with slender flanges. The results summarised in Fig. 22b clearly show a reduction in the stainless steel component of the flexural strength as a result of flange local buckling. To better observe this, the data in Fig. 22a and b for models with  $\lambda_e^w \leq 160$  are replotted in Fig. 22c, this time versus the flange slenderness (i.e.  $\lambda_e^f$  as the x-axis). The figure shows a clear reducing trend after the flange slenderness exceeds 50, which is in line with the assumption made earlier for categorising the compression flange. Further investigation of the results suggested that in CFSST beams with slender flanges, the top flange experiences stresses lower than the yield stress, which could be characterised by its post-local buckling strength. This was in line with the experimental observations of the present study on slender beams (Fig. 10d).

Finally, as shown in Fig. 22d, the flexural resistance exhibited by the concrete infill was investigated. According to the figure, the concrete infill was able to almost always reach to its corresponding plastic moment capacity ( $M_{pl}^{conc}$ ) if the web slenderness was kept below 160. For more slender cases, on the other hand, significant web buckling-induced deformations and the relative slip between concrete and stainless steel limited the strength. In essence, results in Fig. 22a-d suggest the following for CFSSTs under pure bending:

- Webs can be considered compact for all  $\lambda_e^w \leq (\lambda_e^w)_{max} = 160$ .
- A reduction in strength is mainly due to the local buckling of the compression flange when its slenderness ( $\lambda_e^f$ ) exceeds 50.
- The concrete infill can attain its plastic capacity even in highly slender sections, as long as the web slenderness is kept below 160.

Based on these key findings, the following design procedure was recommended for CFSST beams. The flange slenderness is again limited to 140 as discussed earlier:

$$M_{prop} = \begin{cases} M_{pl} & \text{if } \lambda_e^f \leq 50 \\ M_{pb} & \text{if } 50 < \lambda_e^f \leq 140 \end{cases} \quad \text{and for both cases } \lambda_e^w \leq 160 \quad (15)$$

where  $M_{pl}$  is the plastic moment capacity of the CFSST which can easily be determined from a plastic stress distribution, as shown in Fig. 12a, assuming plastic stress blocks for the stainless steel section and the concrete core. It should be noted that the maximum concrete stress ( $f_{c,max}$ ) is conservatively recommended herein as  $\gamma_u f_c$  considering the size effect discussed in the previous section ( $\gamma_u$  from Eq. (12)). For slender cases, on the other hand, the capacity is limited to  $M_{pb}$  which is the *post-local buckling moment capacity* and proposed to be determined using the stress distribution shown in Fig. 12b where the top flange stress is limited to the post-local buckling stress ( $b_e/b$ ) $f_y$  with ( $b_e/b$ ) determined as per Eq. (11), taking  $\lambda_e$  as  $\lambda_e^f$  which is the plate slenderness for the compression flange. For concrete, again a stress block with  $f_{c,max} = \gamma_u f_c$  is recommended. For the sake of completeness, the relevant closed-formed formulae were also derived for both compact CFSST beams:

$$d_{pl}^{NA} = \frac{2Ht_w f_y + bt_f \gamma_u f_c}{4t_w f_y + b \gamma_u f_c} \quad (16)$$

$$M_{pl} = bt_f f_y \left( d_{pl}^{NA} - \frac{t_f}{2} \right) + bt_f f_y \left( H - d_{pl}^{NA} - \frac{t_f}{2} \right) + 2t_w d_{pl}^{NA} f_y \left( \frac{d_{pl}^{NA}}{2} \right) + 2t_w f_y \left( H - d_{pl}^{NA} \right) \left( \frac{H - d_{pl}^{NA}}{2} \right) + b \gamma_u f_c \left( d_{pl}^{NA} - t_f \right) \left( \frac{d_{pl}^{NA} - t_f}{2} \right) \quad (17)$$

and slender CFSST beams:

$$d_{pb}^{NA} = \frac{(b_e/b) \cdot [2Ht_w f_y + (b-b_e)t_f f_y + bt_f \gamma_u f_c]}{[1 + 2(b_e/b) + (b_e/b)^2]t_w f_y + b_e \gamma_u f_c} \quad (18)$$

$$\begin{aligned}
M_{pb} = & b_e t_f f_y \left( d_{pb}^{NA} - \frac{t_f}{2} \right) + b t_f f_y \left( H - d_{pb}^{NA} - \frac{t_f}{2} \right) + 2 t_w d_{pb}^{NA} \left( \frac{b_e}{b} \right) \left( \frac{f_y}{2} \right) \left( \frac{2d_{pb}^{NA}}{3} \right) \\
& + 2 t_w \left( \frac{f_y}{2} \right) \left( \frac{d_{pb}^{NA}}{b_e/b} \right) \left( \frac{2d_{pb}^{NA}}{3b_e/b} \right) + 2 t_w f_y \left( H - d_{pb}^{NA} - \frac{d_{pb}^{NA}}{b_e/b} \right) \left( \frac{H}{2} - \frac{d_{pb}^{NA}}{2} + \frac{1}{2} \frac{d_{pb}^{NA}}{b_e/b} \right) \\
& + b \gamma_u f_c \left( d_{pb}^{NA} - t_f \right) \left( \frac{d_{pb}^{NA} - t_f}{2} \right)
\end{aligned} \quad (19)$$

where  $H$ ,  $b$ ,  $t_w$ ,  $t_f$  as well as the depths of the natural axes ( $d_{pl}^{NA}$  and  $d_{pb}^{NA}$ ) are shown in Fig. 12.

#### 6.2.2. Comparison with design codes and other proposed methods

Most international standards use a plastic stress distribution method (PSDM) similar to that shown in Fig. 12a (considering different  $f_c$  max values though) for the flexural design of compact concrete-filled tubes. Eurocode 4 [60] does not permit the use of slender carbon steel CFSTs. While AS/NZS 2327 [34] provides some information regarding the slenderness limits of these members, it does not address the design of slender CFST beams directly. Clause 4.2.2 of the standard also only addresses the design of *compact* CFSTs under combined loading. It is therefore reasonable to presume both Eurocode 4 and AS/NZS 2327 [34] to be mainly intended for the design of compact CFST beams. AISC 360 [37], on the other hand, provides a full design procedure for compact, noncompact and slender CFSTs. For compact sections ( $\lambda_e^f \leq 64$  and  $\lambda_e^w \leq 85$ ) the plastic stress distribution method is used (Fig. 12a). For ( $64 < \lambda_e^f \leq 85$  or  $85 < \lambda_e^w \leq 161$ ), termed noncompact sections in the American specification, a linear reduction from the plastic moment capacity is considered towards a target strength calculated based on the first-yield moment in steel and a *triangular* concrete stress block with  $f_c$  max =  $0.7f_c$ . For slender sections as per AISC 360 [37] ( $85 < \lambda_e^f \leq 141$ ), a further reduction in strength is considered by limiting the flange stress to a theoretical elastic buckling stress (Fig. 29).

The predictions of the proposed approach (Eqs. (15)–(19)), and those of the specifications, are compared in Fig. 23 to the test and FE results of the present study as well as a limited number of CFSST beam test results available in the literature. The test data was compiled from the experimental results reported previously in the following studies: Yang and Ma [20], Yousif et al. [96], and Chen et al. [22]. It should be noted that the FE results of models with extremely slender webs ( $\lambda_e^w > 160$ ) were not included in the figure based on the earlier discussions. According to Fig. 23a, the method proposed in the present study provides safe results with a reasonable conservatism for the entire range of the dataset. The European and Australian standards (Fig. 23b) provide reasonable results particularly for compact CFSST beams ( $\lambda_e^f \leq 50$ ), however, start to produce unsafe results when higher slenderness values are

approached. This is of course expected since these specifications are mainly intended for compact sections.

Owing to the use of PSDM, the American specification [37] also provides reasonable results for compact cases. However, as shown in Fig. 23c, the conservatism in the predictions tends to increase notably with an increase in the section slenderness. This is a similar issue to that observed for the axial predictions of AISC 360 [37] in Section 6.1.2 (Fig. 21d) and is related to the use of a lower concrete strength ( $0.7f_c$  and a triangular stress distribution) as well as the utilised local buckling curve in AISC 360 (Fig. 20a) which underestimates the strength of plates with high slenderness. It is however important to reiterate that the method in AISC 360 was developed initially for carbon steel CFSTs.

It should be mentioned that methods such as the mixed analysis approach developed by Uy [97] for high-strength carbon steel CFSTs, which uses a partially elastic stress distribution, or that developed in Uy [13], which combines a strain compatibility method with a post-local buckling procedure, can also be incorporated in the CFSST beam design. The method proposed in the present study was in fact built upon these previous studies and calibrated using new test data and analysis results for stainless steel composite members in order to provide a convenient and reliable tool for practicing engineers.

#### 6.3. CFSST section capacity: Axial compression and flexural bending

Interaction diagrams have been traditionally used in international specifications for the design of concrete-filled sections under combined compression and bending [34,37,60]. As shown in Fig. 24a, for compact sections, a plastic stress distribution method (PSDM) can be used to construct the exact interaction diagram. Alternatively, most codes also allow for a simplified PSDM curve to be used in the design, in which, as shown in Fig. 24a, three or four key points of the interaction diagram are first found using predefined plastic stress distributions and then connected together. As shown in the figure, for compact concrete-filled tubes, the main difference between the standards is the use of somewhat different  $f_c$  max values for the concrete stress block ( $f_c$  or  $0.85f_c$ ). In the present study, based on the discussions regarding the size effect (Section 6.1.1), it is proposed to use  $\gamma_u f_c$  in PSDM where  $\gamma_u$  can be readily determined from Eq. (12).

In order to investigate the applicability of the PSDM approach to the design of *compact* CFSSTs under combined actions, the experimental and some of the numerical results of the present study are compared to their corresponding interaction diagrams as shown in Fig. 25. The only other CFSST tests under compression and uniaxial bending were conducted by Uy et al. [18] and the results for one of their specimens are also included in the figure. It should be noted that the nominal concrete strength reported in [18] was utilised for constructing the

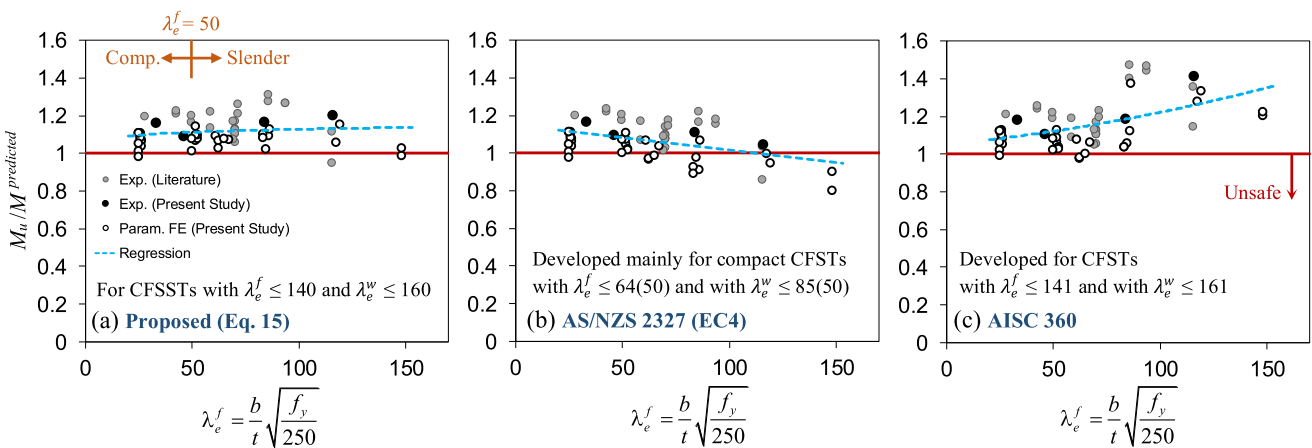
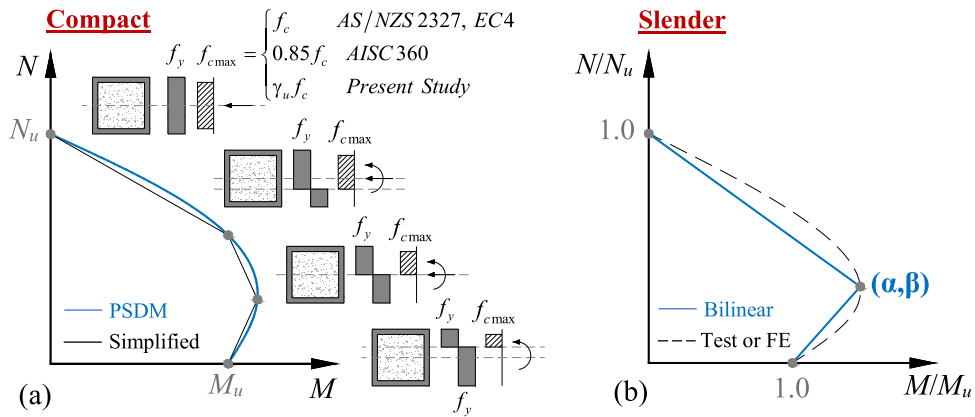


Fig. 23. Comparison of the moment capacities predicted by different approaches with the test and FE results.



**Fig. 24.** Approaches for the design of CFTs under combined loading: (a) compact sections; and (b) slender sections.

interaction diagram. According to the figure, the PSDM approaches used in the Australian, American, and European codes provide reasonable results for compact CFSSTs. Some overestimations can however be observed for the AS/NZS 2327 (or EC4) curve compared to FE results, due to the neglect of the size effect (i.e.  $f_{c\max} = f_c$  in PSDM) which was incorporated in the FE models. As expected, AISC 360 provides the most conservative predictions owing to the use of  $f_{c\max} = 0.85f_c$  in constructing the interaction curves. As it is seen clearly in Fig. 25, the method proposed in the present study moves between the AS/NZS 2327 and AISC 360 curves depending on the section size and the corresponding size effect reduction factor ( $\gamma_u$ ). This allows the recommended method to produce safe and economic results.

The case of slender CFSSTs under combined compression and bending is much more complex as it involves many inter-related concepts. Three approaches are generally considered for designing such sections. The first is to use a method, such as that developed in Uy [13], where a strain compatibility method is combined with a post-local buckling procedure to construct the interaction curve. While an accurate approach, it could be sophisticated for a design office application. In another method, again discussed in Uy [13], slender plates are first substituted with their effective counterparts and then the interaction diagram is constructed using PSDM. This approach is very convenient; however, two issues should be borne in mind. Firstly, effective width relations have not yet been established for webs of CFSSTs which are in contact with concrete. An option would be to instead use the relations developed for hollow stainless steel sections; however, research is needed to substantiate the accuracy of this approach. Secondly, most of the codified methods for determining the effective width of slender plates

under combined loading require an iterative process as they need the properties of the effective section itself in the first place [98]. The procedure can become quite cumbersome if multiple points on the interactions curve are to be determined.

The third approach for designing slender CFTs under combined loading is illustrated in Fig. 24b. In this approach, the anchor points of pure bending and pure compression are first determined. Then, a simplified bilinear interaction diagram is constructed by adding a third anchor point to the diagram, as shown in the figure, which corresponds to the maximum moment point. The coordinates of this third anchor point ( $\alpha, \beta$ ) in the normalised interaction system ( $M/M_u$  vs  $N/N_u$ ) are typically calibrated based on comprehensive numerical simulations which are verified against test data. The method was originally developed by Choi et al. [77] for compact carbon steel CFSTs and later extended to slender CFSTs by Lai et al. [73]. This approach was utilised in the present study considering its healthy balance between practicality and accuracy (which is demonstrated later). As shown by Choi et al. [77], for high confinement factors ( $\xi = A_s f_y / A_c f_c$ ) the third anchor point moves closer to the origin (i.e. the interaction diagram becomes similar to that of a stainless steel section due to higher contribution from the outer tube), whereas for small  $\xi$  values, the point moves away from the origin, increasing the roundness of the interaction diagram (similar to that of a reinforced concrete section). This effect could be clearly observed in the results reported in Fig. 25 as well.

The  $\alpha$  and  $\beta$  coordinates are provided in AISC 360 [37] for slender carbon steel CFSTs based on the study of Lai et al. [73]. In order to propose such relations for slender CFSSTs under combined loading, the  $\alpha$  and  $\beta$  coordinates were extracted for all of the tested and analysed

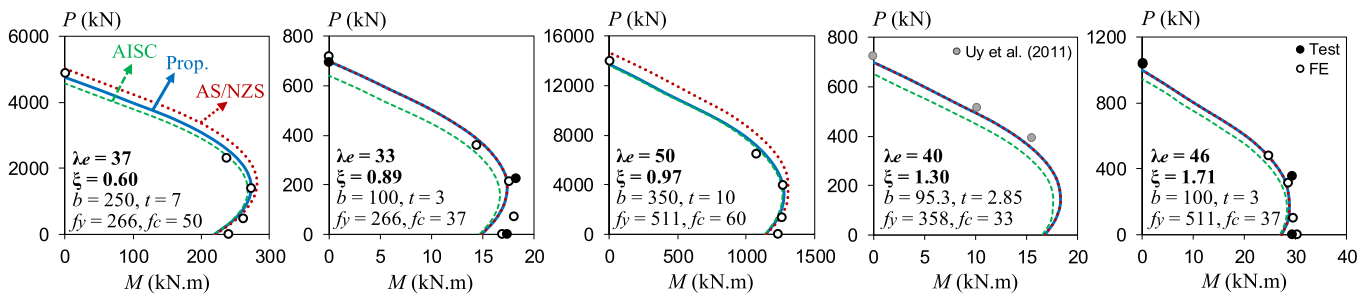


**Fig. 25.** Comparison of the PSDM approaches used in AISC 360, AS/NZS 2327 (= EC4), and the present study with the test and some of the FE results for compact CFSSTs (all dimensions in mm and stresses in MPa).

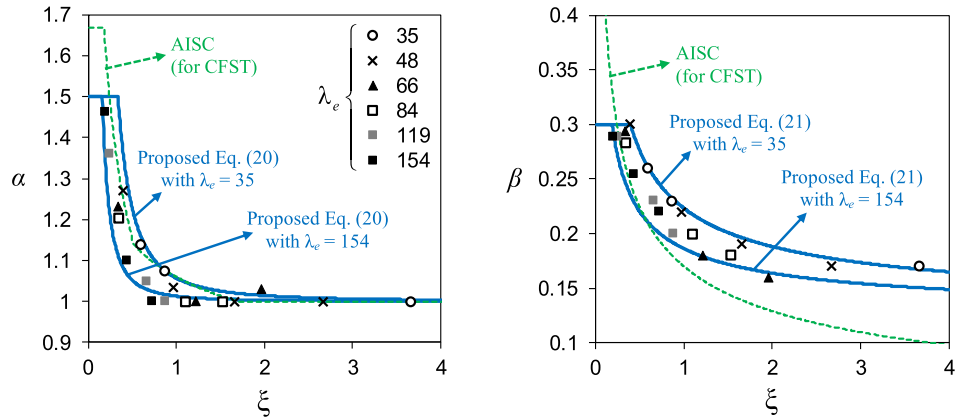
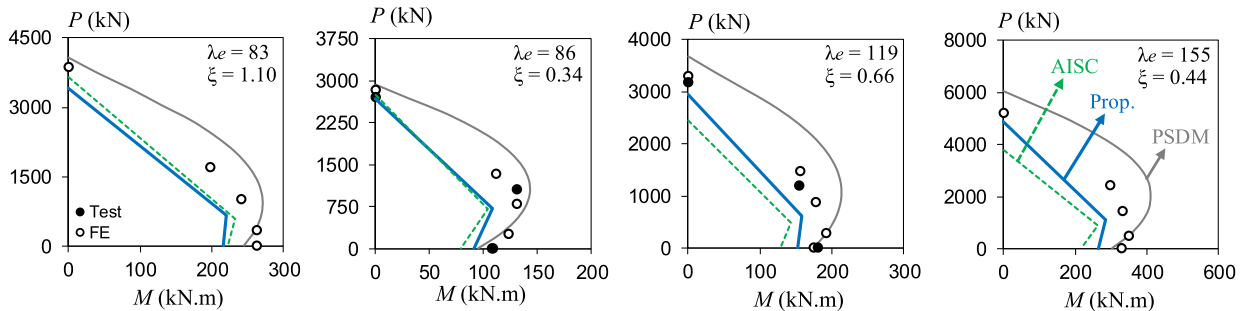
Fig. 26. Regression results for  $\alpha$  and  $\beta$  coordinates.

Fig. 27. Comparison of the predictions of AISC and the method developed herein with the test and some of the FE results for slender CFSSTs.

specimens of the present study and plotted in Fig. 26 against the confinement factor  $\xi$ . The results were then used to calibrate the following formulae:

$$\alpha = 1 + \frac{2}{\lambda_e \xi^2} \leq 1.5 \quad (20)$$

$$\beta = 0.12 + \frac{0.3}{\lambda_e^{0.3} \xi^{0.6}} \leq 0.3 \quad (21)$$

These formulae are compared with the dataset and AISC's equations for slender CFSTs in Fig. 26. The upper limits on  $\alpha$  and  $\beta$  were imposed based on the recommendation of Choi et al. [77]. It should be noted that in AISC the coordinates are solely dependent on  $\xi$  (see Fig. 29), however,

in the present study, a much better correlation with the dataset was obtained with the inclusion of  $\lambda_e$  in the equations. This suggests that the shape of the interaction diagram is influenced not only by  $\xi$ , but also by the plate slenderness ( $\lambda_e$ ) though to a lesser extent.

For the case of combined compression and bending, any CFSST with  $\lambda_e$  larger than 50 was considered slender, where  $\lambda_e$  can conservatively be determined as  $\max(\lambda_e^f, \lambda_e^w)$ . With this categorisation and the above equations in hand, one can readily construct the bilinear  $N$ - $M$  interaction curve for a slender CFSST as follows (Fig. 29):

1. Determine the axial capacity as  $N_{prop}$  using Eq. (13)
2. Determine the flexural capacity as  $M_{prop}$  using Eqs. (15)–(19)
3. Calculate  $\alpha$  and  $\beta$  using Eqs. (20) and (21)
4. Construct the bilinear interaction diagram with three anchor points, namely,  $(0, N_{prop})$ ,  $(\alpha \times M_{prop}, \beta \times N_{prop})$ , and  $(M_{prop}, 0)$

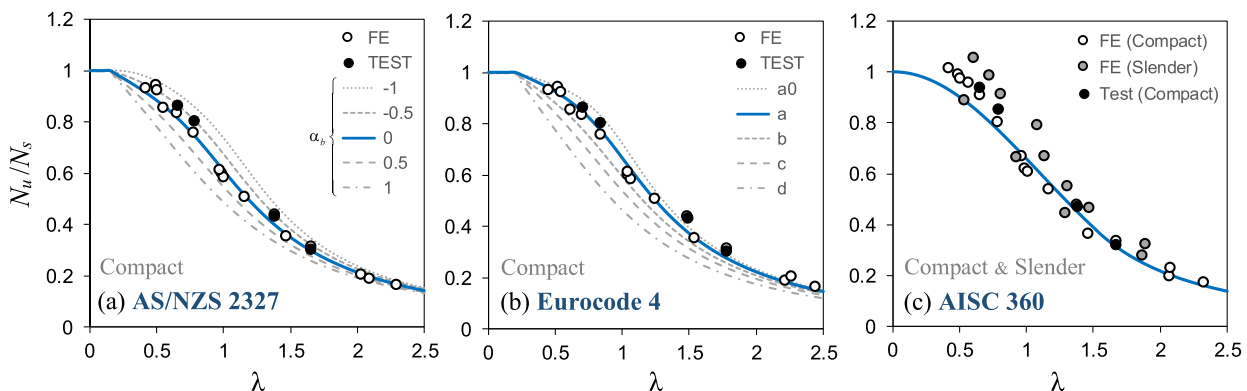


Fig. 28. Comparison of the long column tests and FE analyses with codified column curves.

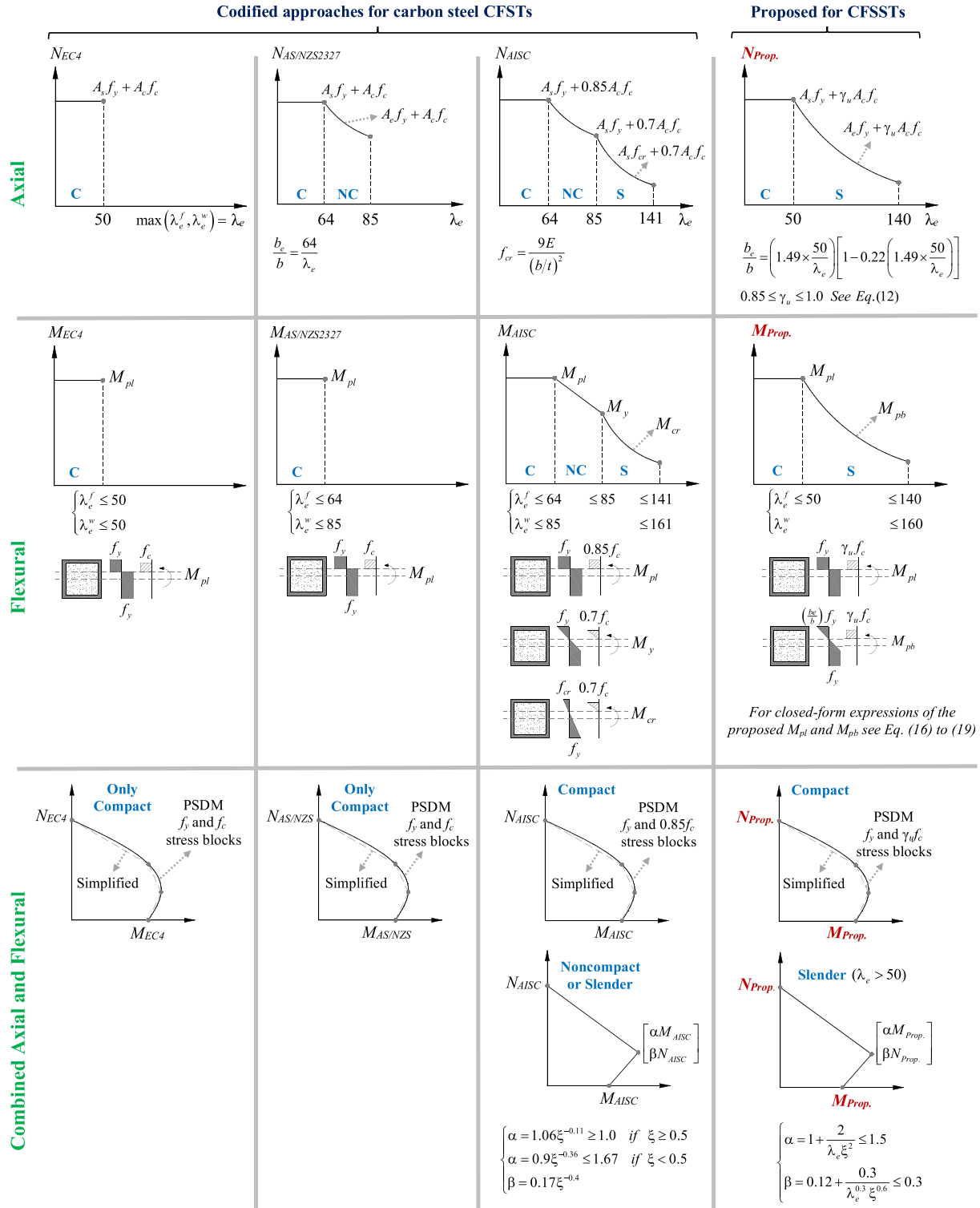


Fig. 29. Summary of the approaches proposed herein for the design of CFSSTs, and the codified design rules for CFSTs.

Interaction diagrams constructed using the outlined approach were compared with the test and FE results of the present study and satisfactory results were found. Some of these comparisons are depicted in Fig. 27. An important issue immediately noted from the figure is the significantly unsafe predictions of the plastic stress distribution method (PSDM) for slender CFSSTs. In contrast, the recommended approach provides safe results with a reasonable degree of conservatism. Its application is also very straightforward. Based on the figure, the proposed

approach and AISC 360 [37] provide relatively similar results for mildly-slender sections, whereas the difference becomes more apparent for sections with higher slenderness ( $\lambda_e$ ) values.

#### 6.4. CFSST member capacity

Global buckling effects are typically included in the design of CFTs using column curves. These curves show the percentage of the reduction

in the compressive strength (with respect to the section strength) versus the relative slenderness ( $\lambda$ ) of the column. Historically, international standards have developed different column curves, and therefore, it is important to investigate their applicability to CFSST columns.

AS/NZS 2327 [34], AISC 360 [37], and Eurocode 4 [60] (which uses the column curves of Eurocode 3 [99]) were considered. Column curves are generally plotted in the ( $\lambda$  vs  $N_u/N_s$ ) coordinate system, where  $N_u$  is the column ultimate load considering global buckling,  $N_s$  is the codified section compressive capacity,  $\lambda = \sqrt{N_s/N_{cr}}$ , is the relative slenderness where  $N_{cr} = \pi^2(EI)_{eff}/L^2$  is the elastic global buckling load,  $(EI)_{eff}$  is the effective flexural stiffness of the composite column taken generally as  $(E_s I_s + \eta E_c I_c)$ , and  $\eta$  is a reduction factor for the concrete stiffness given by each standard:

$$(EI)_{eff} = \begin{cases} E_s I_s + E_c I_c & \text{AS/NZS 2327} \\ E_s I_s + 0.6 E_c I_c & \text{Eurocode 4} \\ E_s I_s + (0.45 \sim 0.9) E_c I_c & \text{AISC 360} \end{cases} \quad (22)$$

The experimental and numerical results of the present study are compared with the codified column curves in Fig. 28. As illustrated in Fig. 28a, AS/NZS 2327 [34] uses a multiple column curve approach considering different values for the section constant  $\alpha_b$ . The data presented in the figure suggested the use of the  $\alpha_b = 0$  curve for the CFSST design as per the Australian standard. This is a lower column curve compared to the  $\alpha_b = -0.5$  curve which is currently in use by the standard for compact carbon steel CFSTs with low or no reinforcement. This observation is in line with the recent study of He et al. [58] on circular CFSSTs.

For the case of Eurocode 4 [60], as shown in Fig. 28b, the results suggested the use of the "a" curve which is currently recommended by the code for carbon steel CFSTs with low or no reinforcement as well. While the column curves of AS/NZS 2327 [34] and Eurocode 4 [60] are identical, the calculation of the relative slenderness ( $\lambda$ ) is different in these specifications due to the use of different  $(EI)_{eff}$  expressions. It is worth noting that the data presented in Fig. 28a,b for AS/NZS 2327 [34] and Eurocode 4 [60] contain only compact sections as the requirements of these codes are primarily developed for such sections. Nevertheless, investigation of the full dataset revealed that the recommended column curves can also be safely used for slender sections provided that the section capacity ( $N_s$ ) is calculated following the recommendations of the present study (Eq. (13) of Section 6.1.1).

As shown in Fig. 28c, AISC 360 [37] uses a single column curve and covers both compact and slender sections. The general performance of the approach was reasonable for compact sections, with some level of overestimation for columns with mid-range relative slenderness values. However, notable underestimation of the capacity can be observed in the figure for columns with slender sections. This was expected since, as discussed in Section 6.1.2, AISC 360 [37] is overly-conservative in determining the section capacity ( $N_s$ ) for slender CFSSTs which in turn affects the  $N_u/N_s$  ratio. This underestimation can readily be avoided by calculating  $N_s$  for slender CFSSTs using Eq. (13) of the present study.

## 7. Summary and conclusions

The paper investigated the behaviour of compact and slender box CFSSTs, fabricated from austenitic and lean duplex materials, under compression, bending, and combined loading, and developed associated design procedures. Such procedures are not currently available for CFSSTs in the literature or design specifications. Results of an experimental programme comprising compact and slender CFSST stub columns and beams, as well as long columns were presented and thoroughly discussed. This was followed by comprehensive numerical simulations considering a very wide range of parameters. A special post-processing technique for separating the loads carried by the stainless steel section and the concrete infill during the tests was developed. The results were then used in a systematic investigation to quantify the stainless steel and concrete components of the

total CFSST resistance. Criteria for categorising compact and slender CFSSTs under axial force, flexure, and combined loading were developed. The obtained experimental and numerical results were then summarised in closed-form design formulae for compact and slender CFSSTs under axial compression or pure bending. The developed procedures accurately accounted for local buckling. The reliability of the formulae was demonstrated by comparison with the results of the present study as well as those available in the literature. The investigation was also extended to the design of compact and slender CFSSTs under combined compression and bending. The unsafe results produced by utilising the plastic stress distribution method for slender CFSSTs under combined loading were highlighted and a simple, yet reliable design method was calibrated. Finally, test and simulation results for long columns were compared against the column curves of international design standards and recommendations were made.

All the recommendations of the present study for the design of box CFSST sections are summarised in Fig. 29. For comparison and completeness, the figure also presents the codified approaches of Eurocode 4 [60], AS/NZS 2327 [34], and AISC 360 [37] which are developed for carbon steel CFSTs. The procedures recommended in the present study can readily be applied in practice.

## Declaration of Competing Interest

The authors declare that they have no known competing financial interests or personal relationships that could have appeared to influence the work reported in this paper.

## Acknowledgments

The study was supported by the Australian Research Council (ARC) under its Discovery Scheme (Project No.: DP180100418). The support provided to the first author by the University of Sydney Postgraduate Award (UPA) is gratefully acknowledged. The austenitic columns were fabricated from plates generously donated by Outokumpu (Mr. Con Logos) and Stirlings Australia (Mr. David Pruden). The technical assistance received from Vulcan (Mr. Stephen Orridge) in regard to the lean duplex plates is also acknowledged. Special thanks to Dr. Jia Wang, Mr. Yuchen Song, Mr. Zhichao Huang, Ms. Yifan Zhou, Mr. Jun Mo, and the technical staff of the J. W. Roderick Laboratory for their assistance during the concrete casting and experiments. The authors also acknowledge the technical support of the Sydney Informatics Hub (SIH) in facilitating the access to Artemis, the high performance computing cluster of the University of Sydney.

## References

- [1] G. Gedge, Structural uses of stainless steel – buildings and civil engineering, *J. Constr. Steel Res.* 64 (11) (2008) 1194–1198.
- [2] N.R. Baddoo, Stainless steel in construction: a review of research, applications, challenges and opportunities, *J. Constr. Steel Res.* 64 (11) (2008) 1199–1206.
- [3] N.R. Baddoo, *AISC Steel Design Guide 27: Structural Stainless Steel*, American Institute of Steel Construction, Chicago, IL, 2013.
- [4] SCI, *Design Manual for Structural Stainless Steel*, 4th ed Steel Construction Institute, Berkshire, UK, 2017.
- [5] AS/NZS 4673, *Cold-Formed Stainless Steel Structures*, Standards Australia/Standards New Zealand, Sydney, Australia/Wellington, New Zealand, 2001.
- [6] Eurocode 3, *Design of steel structures - Part 1-4: General rules - Supplementary rules for stainless steels*, EN 1993-1-4:2006, European Standard, Comité Européen de Normalisation, Brussels, Belgium, 2006.
- [7] International Stainless Steel Forum, *Stainless Steel in Infrastructure: Bridges*, Available Online <https://www.worldstainless.org> 2020.
- [8] L. Gardner, The use of stainless steel in structures, *Prog. Struct. Eng. Mat.* 7 (2) (2005) 45–55.
- [9] S. Afshan, L. Gardner, The continuous strength method for structural stainless steel design, *Thin Wall. Struct.* 68 (2013) 42–49.
- [10] R.W. Furlong, Strength of steel-encased concrete beam columns, *J. Struct. Div. ASCE* 93 (5) (1967) 113–124.

- [11] B. Uy, S.B. Patil, Concrete filled high strength steel box columns for tall buildings: behaviour and design, *Struct. Des. Tall Spec. Build.* 5 (2) (1996) 75–94.
- [12] K. Sakino, H. Nakahara, S. Morino, I. Nishiyama, Behavior of centrally loaded concrete-filled steel-tube short columns, *J. Struct. Eng. ASCE* 130 (2) (2004) 180–188.
- [13] B. Uy, Strength of concrete filled steel box columns incorporating local buckling, *J. Struct. Eng. ASCE* 126 (3) (2000) 341–352.
- [14] L.H. Han, W. Li, R. Bjorhovde, Developments and advanced applications of concrete-filled steel tubular (CFST) structures: members, *J. Constr. Steel Res.* 100 (2014) 211–228.
- [15] A. Roufegarinejad, B. Uy, M.A. Bradford, Behaviour and design of concrete filled steel columns utilizing stainless steel cross sections under combined actions, *Proc. 18th Australasian Conference on the Mechanics of Structures and Materials*, Perth, Australia 2004, pp. 159–165.
- [16] B. Young, E. Ellobody, Experimental investigation of concrete-filled cold-formed high strength stainless steel tube columns, *J. Constr. Steel Res.* 62 (5) (2006) 484–492.
- [17] D. Lam, L. Gardner, Structural design of stainless steel concrete filled columns, *J. Constr. Steel Res.* 64 (11) (2008) 1275–1282.
- [18] B. Uy, Z. Tao, L.H. Han, Behaviour of short and slender concrete-filled stainless steel tubular columns, *J. Constr. Steel Res.* 67 (3) (2011) 360–378.
- [19] D. Lam, J. Yang, X. Dai, Finite element analysis of concrete filled lean duplex stainless steel columns, *Structures* 21 (2019) 150–155.
- [20] Y.F. Yang, G.L. Ma, Experimental behaviour of recycled aggregate concrete filled stainless steel tube stub columns and beams, *Thin Wall. Struct.* 66 (2013) 62–75.
- [21] F.-Y. Liao, C. Hou, W.-J. Zhang, J. Ren, Experimental investigation on sea sand concrete-filled stainless steel tubular stub columns, *J. Constr. Steel Res.* 155 (2019) 46–61.
- [22] Y. Chen, R. Feng, L. Wang, Flexural behaviour of concrete-filled stainless steel SHS and RHS tubes, *Eng. Struct.* 134 (2017) 159–171.
- [23] S. Tokgoz, Tests on plain and steel fiber concrete-filled stainless steel tubular columns, *J. Constr. Steel Res.* 114 (2015) 129–135.
- [24] S. Kazemzadeh Azad, D. Li, B. Uy, Axial Slenderness Limits for Austenitic Stainless Steel-Concrete Composite Columns, *J. Constr. Steel Res.* 166 (2020).
- [25] S. Kazemzadeh Azad, D. Li, B. Uy, Axial slenderness limits for duplex and lean duplex stainless steel-concrete composite columns, *J. Constr. Steel Res.* 172 (2020).
- [26] E. Ellobody, B. Young, Design and behaviour of concrete-filled cold-formed stainless steel tube columns, *Eng. Struct.* 28 (5) (2006) 716–728.
- [27] M.F. Hassanein, Numerical modelling of concrete-filled lean duplex stainless steel tubular stub columns, *J. Constr. Steel Res.* 66 (8–9) (2010) 1057–1068.
- [28] V.I. Patel, Q.Q. Liang, M.N.S. Hadi, Nonlinear analysis of biaxially loaded rectangular concrete-filled stainless steel tubular slender beam-columns, *Eng. Struct.* 140 (2017) 120–133.
- [29] Z. Tao, B. Uy, F.Y. Liao, L.H. Han, Nonlinear analysis of concrete-filled square stainless steel stub columns under axial compression, *J. Constr. Steel Res.* 67 (11) (2011) 1719–1732.
- [30] S. Kazemzadeh Azad, B. Uy, D. Li, C. Hou, A Numerical Study on Local and Post-Local Buckling of Stainless Steel-Concrete Composite Columns, *Proc. 9<sup>th</sup> International Conference on Advances in Steel Structures (ICASS'2018)*, Hong Kong, China, 2018.
- [31] L.H. Han, C.Y. Xu, Z. Tao, Performance of concrete filled stainless steel tubular (CFST) columns and joints: summary of recent research, *J. Constr. Steel Res.* 152 (2019) 117–131.
- [32] B. Uy, Local and post-local buckling of concrete filled steel welded box columns, *J. Constr. Steel Res.* 47 (1) (1998) 47–72.
- [33] R.Q. Bridge, M.D. O'Shea, Behaviour of thin-walled steel box sections with or without internal restraint, *J. Constr. Steel Res.* 47 (1) (1998) 73–91.
- [34] AS/NZS 2327:2017, (+Am1:2020) *Composite structures – Composite steel-concrete construction in buildings*, Standards Australia/Standards New Zealand, Sydney, Australia/Wellington, New Zealand, 2020.
- [35] Eurocode 3, *Design of steel structures - Part 1-4: General rules - Supplementary rules for stainless steels*, EN 1993-1-4:2006 +A1:2015, European Standard, Comité Européen de Normalisation, Brussels, Belgium, 2006 (+A1:2015).
- [36] Eurocode 3, *Design of steel structures - Part 1-1: general rules and rules for buildings*, EN 1993-1:2003, European Standard, Comité Européen de Normalisation, Brussels, Belgium, 2003.
- [37] AISC, *Specification for Structural Steel Buildings*, ANSI/AISC 360–16, American Institute of Steel Construction, Chicago, IL, 2016.
- [38] H.X. Yuan, Y.Q. Wang, Y.J. Shi, L. Gardner, Stub column tests on stainless steel built-up sections, *Thin Wall. Struct.* 83 (2014) 103–114.
- [39] AS 1391, *Metallic materials – Tensile testing at ambient temperature*, Standards Australia, Sydney, Australia, 2007.
- [40] Y. Huang, B. Young, The art of coupon tests, *J. Constr. Steel Res.* 96 (2014) 159–175.
- [41] AS 1012, *Methods of testing concrete*, Standards Australia, Sydney, Australia, 2014.
- [42] B.W. Schafer, T. Peköz, Computational modeling of cold-formed steel: characterizing geometric imperfections and residual stresses, *J. Constr. Steel Res.* 47 (3) (1998) 193–210.
- [43] X. Zhao, M. Toorkaboni, B.W. Schafer, Laser-based cross-section measurement of cold-formed steel members: model reconstruction and application, *Thin Wall. Struct.* 120 (2017) 70–80.
- [44] V. Zeinoddini, B.W. Schafer, Global imperfections and dimensional variations in cold-formed steel members, *Int. J. Struct. Stab. Dyn.* 11 (05) (2011) 829–854.
- [45] N. Boissonade, K. Weynand, J.-P. Jaspart, Application of new Eurocode 3 formulae for beam-columns to Class 3 hollow section members, *Proc. 12th International Symposium on Tubular Structures*, Shanghai, China, 2008.
- [46] K.J.R. Rasmussen, G.J. Hancock, Tests of high strength steel columns, *J. Constr. Steel Res.* 34 (1) (1995) 27–52.
- [47] AS/NZS 5131, *Structural steelwork – Fabrication and erection*, Standards Australia/Standards New Zealand, Sydney, Australia/Wellington, New Zealand, 2016.
- [48] EN 1090-2, *Execution of steel structures and aluminium structures – Part 2: Technical requirements for steel structures* – EN 1090-2:2008, European Standard, Comité Européen de Normalisation, Brussels, 2008.
- [49] AISC, *Code of Standard Practice for Structural Stainless Steel Buildings*, AISC 313 (Draft), American Institute of Steel Construction, Chicago, IL, 2020.
- [50] A. Xiamuxi, A. Hasegawa, Load-sharing ratio analysis of reinforced concrete filled tubular steel columns, *Steel Compos. Struct.* 12 (6) (2012) 523–540.
- [51] Z. Lai, A.H. Varma, High-strength rectangular CFT members: database, modeling, and design of short columns, *J. Struct. Eng. ASCE* 144 (5) (2018) 04018036.
- [52] B. Uy, Confinement effects and slenderness limits for square concrete-filled steel columns using high strength steel, *Proc. 5th European Conference on Steel and Composite Structures (EUROSTEEL 2008)*, Graz, Austria, 2008.
- [53] H.-S. Hu, Y. Liu, B.-T. Zhuo, Z.-X. Guo, B.M. Shahrooz, Axial compressive behavior of square CFST columns through direct measurement of load components, *J. Struct. Eng. ASCE* 144 (11) (2018) 04018201.
- [54] J.C. Simo, T.J.R. Hughes, *Computational Inelasticity*, Springer-Verlag, New York, 1998.
- [55] L.L. Yaw, *Nonlinear Static - 1D Plasticity - Various Forms of Isotropic Hardening*, Walla Walla University, 2012.
- [56] M. Kojic, K.J. Bathe, *Inelastic Analysis of Solids and Structures*, Springer-Verlag, New York, 2004.
- [57] L.-H. Han, Flexural behaviour of concrete-filled steel tubes, *J. Constr. Steel Res.* 60 (2) (2004) 313–337.
- [58] A. He, Y. Liang, O. Zhao, Flexural buckling behaviour and resistances of circular high strength concrete-filled stainless steel tube columns, *Eng. Struct.* 219 (2020) 110893.
- [59] C. Buchanan, E. Real, L. Gardner, Testing, simulation and design of cold-formed stainless steel CHS columns, *Thin Wall. Struct.* 130 (2018) 297–312.
- [60] Eurocode 4, *Design of composite steel and concrete structures – Part 1-1: General rules and rules for buildings*, EN 1994-1-1:2004, European Standard, Comité Européen de Normalisation, Brussels, Belgium, 2004.
- [61] H.-S. Hu, J.-G. Nie, Y.-H. Wang, Effective stiffness of rectangular concrete filled steel tubular members, *J. Constr. Steel Res.* 116 (2016) 233–246.
- [62] ABAQUS 6.14-1 Documentation, Dassault Systèmes, Simulia, Providence, RI, 2014.
- [63] Z. Tao, Z.-B. Wang, Q. Yu, Finite element modelling of concrete-filled steel stub columns under axial compression, *J. Constr. Steel Res.* 89 (2013) 121–131.
- [64] T. Yu, J.G. Teng, Y.L. Wong, S.L. Dong, Finite element modeling of confined concrete-II: plastic-damage model, *Eng. Struct.* 32 (3) (2010) 680–691.
- [65] L.-H. Han, G.-H. Yao, Z. Tao, Performance of concrete-filled thin-walled steel tubes under pure torsion, *Thin Wall. Struct.* 45 (1) (2007) 24–36.
- [66] S. Kazemzadeh Azad, B. Uy, Effect of concrete infill on local buckling capacity of circular tubes, *J. Constr. Steel Res.* 165 (2020) 105899.
- [67] Z. Huang, B. Uy, D. Li, J. Wang, Behaviour and design of ultra-high-strength CFST members subjected to compression and bending, *J. Constr. Steel Res.* 175 (2020) 106351.
- [68] CEB-FIP, *CEB-FIP Model Code*, 1993, Thomas Telford, London, 1990.
- [69] H.X. Yuan, Y.Q. Wang, Y.J. Shi, L. Gardner, Residual stress distributions in welded stainless steel sections, *Thin Wall. Struct.* 79 (2014) 38–51.
- [70] H. Ban, G. Shi, Y. Shi, Y. Wang, Overall buckling behavior of 460MPa high strength steel columns: experimental investigation and design method, *J. Constr. Steel Res.* 74 (2012) 140–150.
- [71] R.D. Ziemian, *Guide to Stability Design Criteria for Metal Structures*, 6th ed. John Wiley & Sons, Hoboken, NJ, 2010.
- [72] J. Zhang, M.D. Denavit, J.F. Hajjar, X. Lu, Bond behavior of concrete-filled steel tube (CFT) structures, *Eng. J. AISC* 49 (4) (2012) 169–186.
- [73] Z. Lai, A.H. Varma, L.G. Griffis, Analysis and design of noncompact and slender CFT beam-columns, *J. Struct. Eng. ASCE* 142 (1) (2016) 04015097.
- [74] Z. Lai, A.H. Varma, K. Zhang, Noncompact and slender rectangular CFT members: experimental database, analysis, and design, *J. Constr. Steel Res.* 101 (2014) 455–468.
- [75] L.H. Han, G.H. Yao, X.L. Zhao, Tests and calculations for hollow structural steel (HSS) stub columns filled with self-consolidating concrete (SCC), *J. Constr. Steel Res.* 61 (9) (2005) 1241–1269.
- [76] M. Khan, B. Uy, Z. Tao, F. Mashiri, Behaviour and design of short high-strength steel welded box and concrete-filled tube (CFT) sections, *Eng. Struct.* 147 (2017) 458–472.
- [77] Y.-H. Choi, D.A. Foutch, J.M. LaFave, New approach to AISC P-M interaction curve for square concrete filled tube (CFT) beam-columns, *Eng. Struct.* 28 (11) (2006) 1586–1598.
- [78] L.-H. Han, X.-L. Zhao, Z. Tao, Tests and mechanics model for concrete-filled SHS stub columns, columns and beam-columns, *Steel Compos. Struct.* 1 (1) (2001) 51–74.
- [79] GB 50010–2010, *Code for Design of Concrete Structures*, Ministry of Housing and Urban-Rural Development, Beijing, 2010.
- [80] AS 3600, *Concrete structures*, Standards Australia, Sydney, Australia, 2018.
- [81] Eurocode 2, *Design of concrete structures - Part 1-1: General rules and rules for buildings*, EN 1992-1-1:2003, European Standard, Comité Européen de Normalisation, Brussels, Belgium, 2003.
- [82] H.T. Thai, B. Uy, M. Khan, Z. Tao, F. Mashiri, Numerical modelling of concrete-filled steel box columns incorporating high strength materials, *J. Constr. Steel Res.* 102 (2014) 256–265.
- [83] A. He, F. Wang, O. Zhao, Experimental and numerical studies of concrete-filled high-chromium stainless steel tube (CFHSST) stub columns, *Thin Wall. Struct.* 144 (2019) 106273.
- [84] R.F. Blanks, C.C. McNamara, Mass concrete tests in large cylinders, *ACI J. Proc.* 31 (1) (1935) 280–303.

- [85] Z.P. Bažant, Size effect in blunt fracture: concrete, rock, metal, *J. Eng. Mech. ASCE* 110 (4) (1984) 518–535.
- [86] J.-K. Kim, S.-T. Yi, C.-K. Park, S.-H. Eo, Size effect on compressive strength of plain and spirally reinforced concrete cylinders, *ACI Struct. J.* 96 (1) (1999) 88–94.
- [87] F. Aslani, Effects of specimen size and shape on compressive and tensile strengths of self-compacting concrete with or without fibres, *Mag. Conc. Res.* 65 (15) (2013) 914–929.
- [88] M. Mursi, B. Uy, Strength of slender concrete filled high strength steel box columns, *J. Constr. Steel Res.* 60 (12) (2004) 1825–1848.
- [89] S.P. Schneider, Axially loaded concrete-filled steel tubes, *J. Struct. Eng. ASCE* 124 (10) (1998) 1125–1138.
- [90] T. Yamamoto, J. Kawaguchi, S. Morino, Experimental Study of Scale Effects on the Compressive Behavior of Short Concrete-Filled Steel Tube Columns, *Proc. Composite Construction in Steel and Concrete IV*, Alberta, Canada, 2002.
- [91] T. Fujimoto, A. Mukai, I. Nishiyama, K. Sakino, Behavior of eccentrically loaded concrete-filled steel tubular columns, *J. Struct. Eng. ASCE* 130 (2) (2004) 203–212.
- [92] Y. Wang, P. Chen, C. Liu, Y. Zhang, Size effect of circular concrete-filled steel tubular short columns subjected to axial compression, *Thin Wall. Struct.* 120 (2017) 397–407.
- [93] Q.Q. Liang, Performance-based analysis of concrete-filled steel tubular beam-columns, part I: theory and algorithms, *J. Constr. Steel Res.* 65 (2) (2009) 363–372.
- [94] D. Lam, J. Yang, A. Mohammed, Axial behaviour of concrete filled lean duplex stainless steel square hollow sections, *Proc. 8th European Conference on Steel and Composite Structures (Eurosteel 2017)*, Copenhagen, Denmark, 2017.
- [95] S.A. Mirza, E.A. Lacroix, Comparative strength analyses of concrete-encased steel composite columns, *J. Struct. Eng. ASCE* 130 (12) (2004) 1941–1953.
- [96] M. Yousuf, B. Uy, Z. Tao, A. Remennikov, J.Y.R. Liew, Transverse impact resistance of hollow and concrete filled stainless steel columns, *J. Constr. Steel Res.* 82 (2013) 177–189.
- [97] B. Uy, Strength of short concrete filled high strength steel box columns, *J. Constr. Steel Res.* 57 (2) (2001) 113–134.
- [98] Eurocode 3, Design of steel structures – Part 1–5: Plated structural elements, EN 1993-1-5:2006, European Standard, Comité Européen de Normalisation, Brussels, Belgium, 2006.
- [99] Eurocode 3, Design of steel structures – Part 1–1: General rules and rules for buildings, EN 1993-1-1:2005, European Standard, Comité Européen de Normalisation, Brussels, Belgium, 2005.